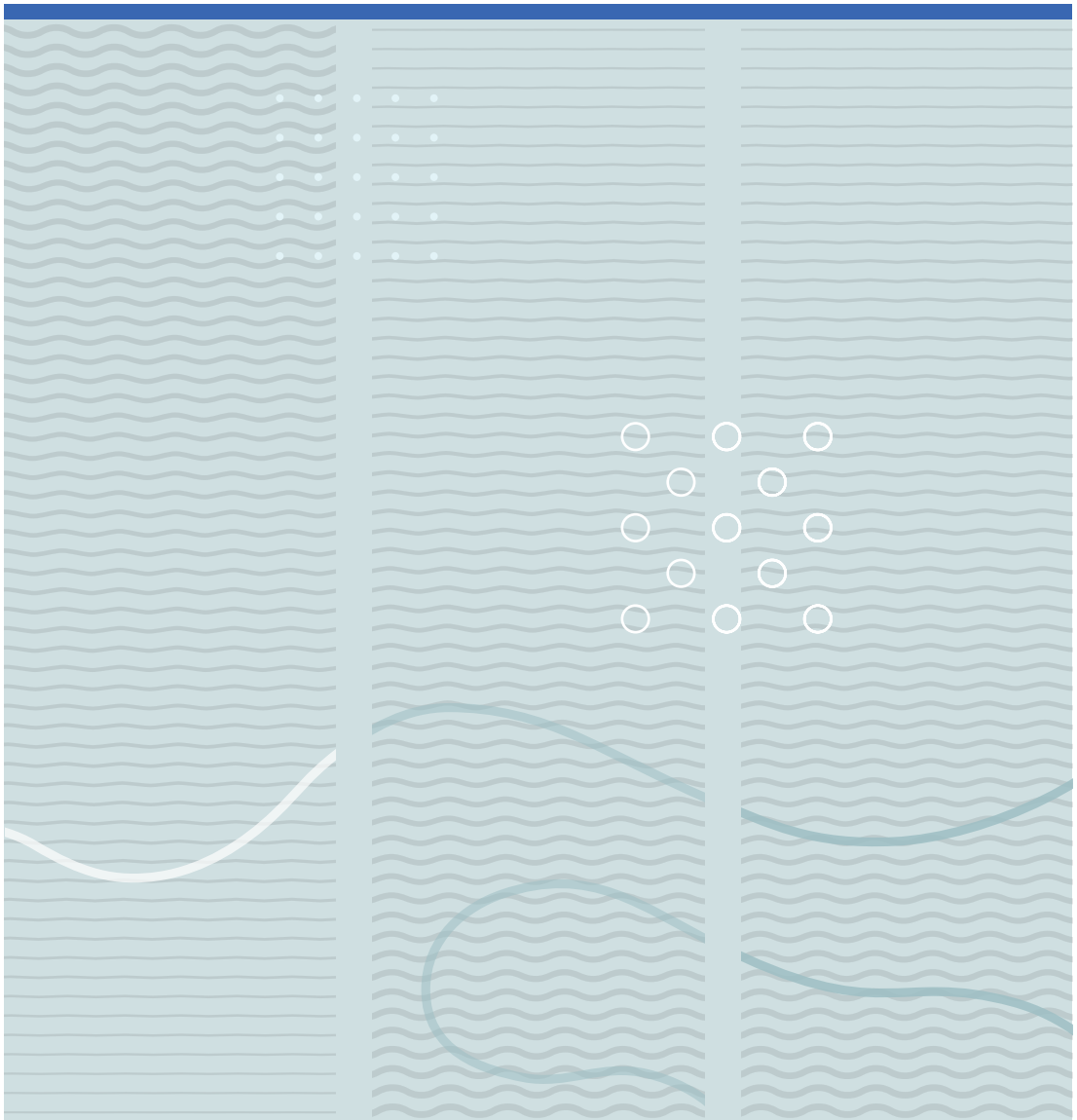Kang Du

Heterojunction Engineering on TiO$_2$ Nanotubes Electrodes and Their Applications

US**N**

Kang Du

Heterojunction Engineering on TiO$_2$ Nanotubes Electrodes and Their Applications

A PhD dissertation in
Applied Micro- and Nanosystems

Preface

This doctoral thesis is submitted for the degree of Doctor of Philosophy at the Faculty of Technology and Maritime Science, University of South-Eastern Norway (USN), Norway.

This doctoral work had been carried out from September 2014 to August 2017 at Department of Microsystems (USN) under the supervision of Professor Kaiying Wang and Professor Xuyuan Chen.

Acknowledgments

First and foremost, I would like to express sincere to principal supervisor Professor Kaiying Wang and assistance supervisor Professor Xuyuan Chen for their invaluable guidance, constructive advice, and endless support during my Ph. D research.

I would also like to give thanks to Zekija Ramic, Ragnar D. Johansen, Thomas Martinsen, Muhammad Tayyib, Thai Anh Tuan Nguyen and Birgitte Kasin Hønsvall of IMS-USN, Joachim Seland Graff and Annett Thøgersen of SINTEF, Klaus Magnus Haland Johansen, Heine Nygard Riise, and Wei Zhan of UiO for their experimental helps.

My appreciations are also expressed to the colleagues at the Department of Microsystems at USN for their facilities and administrative assistance. Special thanks Dr. Guohua Liu, Dr. Ying Zhao, Dr. Pai Lu, Mr. Chaoqun Cheng, Mr. Zengxing Zhang, Mr. Xiao Fan, Mrs. Yingge Wang, Mr. Chengjun Yu, and master students Mr. Rongteng Lu, Mrs. Qi Zhang, Mr. Shuai Zhang, Mrs. Shirou Tang, Mr. Fan Chen, Mr. Kim Robert Gustavsen.

Finally, I am thankful for my parents, wife, and friends for their love, encouragement, and support.

Abstract

With the dramatic progress in nanotechnology, TiO$_2$ nanomaterials have shown blooming applications in the field of energy and environment since the discovery of water photolysis on a TiO$_2$ electrode in 1972. In particular, TiO$_2$ nanotubes (TNT) exhibit the superior performance owing to their inherent properties of unique morphologies, electronic, physical, and chemical properties. However, several intrinsic drawbacks of TNT (such as white color, poor conductivity, and wide bandgap) still limit their visible light absorption, charge generation, separation, and transport, and eventually, lead to a low photoelectrochemical (PEC) performance in the practical applications.

This Ph. D thesis focuses on the following challenges: (1) explore the methods for enhancing the absorption of TNT in visible light regime; (2) investigate the approaches to improve the conductivity of TNT; (3) probe the strategies for suppressing the charge recombination of TNT; (4) develop the applications of TNT-based electrodes. The achievements towards these challenges are summarized below.

Article 1 reported the synthesis of PbS QDs/TNT heterogenous electrode by ultrasonic-assisted dip-coating technique. PbS QDs/TNT shows an enhanced absorption in visible regime, and its photocurrent density is increased under the illumination as well. The enhanced I-V characteristics are well interpreted by charge generation, separation, and transport in the heterojunction band diagrams of PbS QDs/TNT system.

Article 2 introduced a facile process to synthesize Ti^{3+}/TNT heterojunction electrode by electrochemical reduction method. An excellent capacitive performance has been observed for the heterojunction electrode due to the formation of Ti^{3+} sites on the TNT surface. Its specific capacitance is further increased by a controllable morphology modification through ultrasonic treatment. Also, electrochemical impedance spectroscopy (EIS) demonstrates that Ti^{3+}/TNT possesses a higher conductivity and is beneficial to charge transport.

Article 3 presented the preparation of TiN/TNT heterojunction electrode by conformally coating TiN layer through ALD technique. Cyclic voltammetry (CV) and electrochemical

impedance spectroscopy (EIS) analysis show that TiN/TNT has higher capacitance and lower equivalent series resistance (ESR) than that of pristine TNT. The TiN/TNT heterojunction electrode exhibits a potential for high-performance electrode material of energy storage devices.

Article 4 investigated the PEC properties of the synthesized "black" Ti^{3+}/TNT heterojunction electrode. UV-Vis spectrum indicates that Ti^{3+}/TNT has a strong absorption in the visible region. The enhanced photocurrent densities are well explained by high efficient charge generation and transport under visible illumination. Besides, CdSe QDs are loaded on Ti^{3+}/TNT by a dip-coating technique for further improving charge separation.

Article 5 described the development of MoS$_2$/CdS/TNT heterojunction electrode by magnetron sputtering technique. The as-prepared electrode possesses superior photochemical activity on CO$_2$ conversion, showing the enhanced yields on the generation of H$_2$, CO, and CH$_4$. A possible mechanism for the improved photocatalytic activity is attributed to enhancing light absorption, accelerating carrier separation, and offering active edge sites.

Article 6 studied the charge separation and transport properties on PbS QDs/Au/Ti^{3+}/TNT heterojunction nanocomposites which are synthesized by magnetron sputter and subsequently dip coating approach. The PEC characteristics of PbS QDs/Au/Ti^{3+}/TNT reveal that the loadings of Au NPs and PbS QDs on Ti^{3+}/TNT are used as separation centers rather than light absorbers for suppressing charge recombination.

Keywords: solar energy, TiO$_2$ nanotubes, heterojunction engineering, energy conversion.

Papers omitted from online edition due to publishers restrictions

List of papers

Article 1

Kang Du, Guohua Liu, Xuyuan Chen, and Kaiying Wang. PbS Quantum Dots Sensitized TiO_2 Nanotubes for Photocurrent Enhancement. Journal of The Electrochemical Society 162, no. 10 (2015): E251-E257. DOI: 10.1149/2.0661510jes.

My contribution: electrodes synthesis, characterization, measurement, manuscript preparation.

Article 2

Kang Du, Guohua Liu, Mengwei Li, Chenggen Wu, Xuyuan Chen, and Kaiying Wang. Electrochemical reduction and capacitance of hybrid titanium dioxides—nanotube arrays and "nanograss". Electrochimica Acta 210 (2016): 367-374. DOI: 10.1016/j.electacta.2016.05.027.

My contribution: electrodes synthesis, characterization, measurement, manuscript preparation.

Article 3

Kang Du, Pai Lu, Guohua Liu, Xuyuan Chen, and Kaiying Wang. Atomic layer deposition of TiN layer on TiO_2 nanotubes for enhanced supercapacitor performance. 19th International Conference on Solid-State Sensors, Actuators and Microsystems (TRANSDUCERS), (2017): 710-713. DOI**:** 10.1109/TRANSDUCERS.2017.7994147.

My contribution: electrodes synthesis, characterization, measurement, manuscript preparation.

Article 4

Kang Du, Guohua Liu, Xuyuan Chen, and Kaiying Wang. Photocurrent Properties of Ti^{3+} Introduced TiO_2 Nanotubes Photoelectrode Decorated by CdSe Quantum Dots. ECS Transactions 77, no. 6 (2017): 107-118. DOI: 10.1149/07706.0107ecst.

My contribution: electrodes synthesis, characterization, measurement, manuscript preparation.

Article 5

Kang Du, Guohua Liu, Xuyuan Chen, and Kaiying Wang, Nanotube Heterostructures MoS$_2$/CdS/TiO$_2$ for CO$_2$ conversion, ECS Transactions 85, no. 10 (2018) 47-56. DOI: 10.1149/08510.0047ecst.

My contribution: electrodes synthesis, characterization, measurement, manuscript preparation.

Article 6

Kang Du, Guohua Liu, Xuyuan Chen, and Kaiying Wang, Fast Charge Separation and Photocurrent Enhancement on Black TiO$_2$ Nanotubes co-sensitized with Au Nanoparticles and PbS Quantum Dots, Electrochimica Acta 277 (2018): 244-254. DOI: https://doi.org/10.1016/j.electacta.2018.05.014.

My contribution: electrodes synthesis, characterization, measurement, manuscript preparation.

Papers not enclosed in the thesis

Article 7

Kang Du, Guohua Liu, Xuyuan Chen, and Kaiying Wang. Photocurrent Enhancement of TiO$_2$ Nanotubes Decorated with PbS Quantum Dots. ECS Transactions 66, no. 1 (2015): 305-312. DOI: 10.1149/06601.0305ecst.

Article 8

Kang Du, Guohua Liu, Haisheng San, Xuyuan Chen, and Kaiying Wang. PbS Quantum Dots and Au Nanoparticle Co-Sensitized Black TiO$_2$ Nanotubes for Photocurrent Enhancement. ECS Transactions 75, no. 1 (2016): 125-134. DOI: 10.1149/07501.0125ecst.

Article 9

Kang Du, Guohua Liu, Xuyuan Chen, and Kaiying Wang, High-Performance Symmetry Supercapacitors based on TiO$_2$ nanotubes coated Titanium Nitride Layer by ALD technique, in preparation.

Article 10

Kang Du, Guohua Liu, Xuyuan Chen, and Kaiying Wang, Reversible Ti^{3+}/Ti^{4+} redox conversion for recoverable supercapacitors, in preparation.

Article 11

Guohua Liu, Kang Du, and Kaiying Wang. Surface wettability of TiO$_2$ nanotube arrays prepared by electrochemical anodization. Applied Surface Science 388 (2016): 313-320. DOI: 10.1016/j.apsusc.2016.01.010.

Article 12

Guohua Liu, Kang Du, Jinliang Xu, Guang Chen, Mingyan Gu, Changping Yang, Kaiying Wang, and Henrik Jakobsen. Plasmon-dominated photoelectrodes for solar water splitting. Journal of Materials Chemistry A 5, no. 9 (2017): 4233-4253. DOI: 10.1039/C6TA10471A

Article 13

Guohua Liu, Kang Du, Sophia Haussener, and Kaiying Wang. Charge Transport in Two-Photon Semiconducting Structures for Solar Fuels. ChemSusChem No. 9, 20, (2016): 2878–2904. DOI: 10.1002/cssc.201600773.

Article 14

Pai Lu, Kang Du, Per Ohlckers, Einar Halvorsen, Lutz Müller, Steffen Leopold, Martin Hoffmann et al. Silicon grass based nano functional electrodes for MEMS supercapacitors of improved energy density. 19th International Conference on Solid-State Sensors, Actuators and Microsystems (TRANSDUCERS), (2017): 1828-1831. DOI: 10.1109/TRANSDUCERS.2017.7994425.

List of Figures

Abbreviations

AFM	Atomic Force Microscope
ALD	Atomic Layer Deposition
AIDS	Acquired Immune Deficiency Syndrome
BID	Barrier Ionization Discharge
CB	Conduction Band
CV	Cyclic Voltammetry
DSSC	Dye-Sensitized Solar Cell
DI	Deionized
EDLC	Electronic Double Layer Capacitor
EIS	Electrochemical Impedance Spectroscopy
EDX	Energy-dispersive X-ray spectroscopy
ESR	Equivalent Series Resistances
FTO	Fluorine-doped Tin Oxide
GC	Gas Chromatography
HEI	Hot electron injection
HIV	Human Immunodeficiency Virus
HRTEM	High-Resolution Transmission Electron Microscope
NASA	National Aeronautics and Space Administration
NHE	Normal Hydrogen Electrode
NIR	Near Infrared
NO$_x$	Nitrogen Oxides
NPs	Nanoparticles
OA	Oleic Acid
PEC	Photoelectrochemical
PM	Particulate Matter
PRET	Plasmonic resonance energy transfer
PV	Photovoltaics
QDs	Quantum Dots

RWGS	Reverse Water Gas Shift
SEM	Scanning Electron Microscope
SO$_x$	Sulfur Oxides
STEM	Scanning Transmission Electron Microscope
TEM	Transmission Electron Microscope
TNT	TiO$_2$ nanotubes
UV	Ultraviolet
VB	Valence Band
VOCs	Volatile Organic Compounds
WGS	Water Gas Shift
WHO	World Health Organization

List of Symbols

e^-	Electron
h^+	Hole
E^0	Vacuum Level
E_c	Conduction Band
E_f	Fermi Level
E_g	Band Gap
E_v	Valence Band
E_{photon}	Photon Energy
H^+	Hydrogen Ion
hv	Photon energy
q	Electron Charge
Φ_F	Work Function of FTO
Φ_T	Work Function of Titanium

Table of contents

1 Introduction

1.1 Background

Both population growth (reaching an estimated 9.8 billion by 2050) and increasing standards of living for many people will get rise to strong growth in energy demand [1-2]. At present, more than ~80 percent of world energy consumption is produced using fossil fuels (coal, petroleum, and natural gas) [3-5]. The burning of fossil fuels generates pollutants (SO$_x$, NO$_x$, PM, CO, VOCs, and CO$_2$, etc.) that cause severe environmental problems and air pollution [6-7]. For example, the global warming problem is mainly caused by the emission of CO$_2$ and average global surface temperatures in the first six months of 2017 are 0.94 °C above the 1950-1980 average, according to NASA [8]. Besides, the number of deaths attributed to air pollution each year is 6.5 million, much higher than the number from HIV/AIDS, tuberculosis and road injuries combined, based on the data of World Health Organization (WHO) [9].

Nowadays, energy and environment issues appear to be an important challenge for our society since the first industrial revolution [10]. The world needs another revolution to make our resources of energy affordable, accessible and sustainable [11-12]. For this regard, developing renewable energy (such as solar [13], wind [14], waves [15], and geothermal heat [16], etc.) appear to be the most efficient and effective solutions. Solar energy is considered as the most plentiful and ubiquitous source available on the Earth because the energy from sunlight stroked on the Earth within 1 hour is more than the total world energy consumed by humans in an entire year [17]. However, solar energy is an intermittent and variable resource on the Earth which could not supply reliable energy for a system run in a long time.

In a traditional application, solar energy is captured by two engineering models (photovoltaics (PV) cells [18] and solar collectors [19]) and convert it into electricity or heat energy. However, these forms of energies are in low conversion-efficiency and need high cost for storage or transportation. In fact, the natural process of

photosynthesis can turn sunlight and water into carbohydrate, achieving solar energy capture, conversion and storage, but its efficiency is excruciatingly low. Inspired by this natural process, researchers are pursuing the ways to convert solar energy into useful forms. Solar fuels are a game-changer technology to produce chemical fuels by using sunlight to drive chemical reactions (such as, artificial photosynthesis [20], thermochemical [21], or electrochemical reaction [22] etc.) and then store solar energy in the form of chemical bonds (such as H_2, CO, CH_4, and CH_3OH, etc.) for later usage. Figure 1-1 shows schematic for solar fuels production [23].
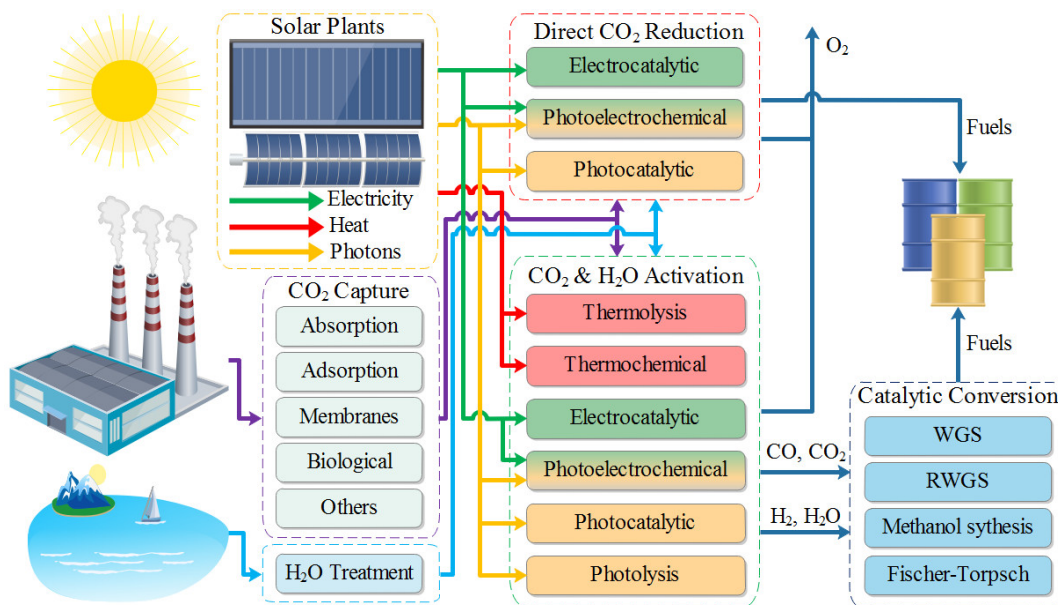
Figure 1-1 Schematic for solar fuels production.

Solar fuels show distinct advantages: firstly, the production of solar fuels solves the conversion and storage problems simultaneously. Secondly, solar fuels are easy to store compared with electricity or heat, and their energy densities (compressed H_2: ~40,000 Wh/Kg, liquefied natural gas: ~15,000 Wh/Kg) are dozens of times than that of the electricity storage devices (Li-ion batteries: ~300 Wh/Kg, Supercapacitors: ~10 Wh/Kg). Thirdly, solar fuels are liable to transport rather than build a complex distribution network. Furthermore, CO_2 can be used as one of the feedstocks for synthesizing solar fuels, facilitating to reduce the emission of CO_2. For the production of the solar fuels, materials are the most important challenge for the development of all technologies [24].

Specifically, the ever-increasing growth of research activities in nanoscience and nanotechnology continually brings new physical and chemical properties on nanomaterials, which may play a significant role in promoting a step-change breakthrough to cost-effective solar fuels conversion, storage, and utilization [25].

1.2 Titanium Dioxides

Titanium dioxides (TiO_2) was first used as a white pigment since its commercial production in the 1920s [26]. Until in the early 1970s, the pioneers Fujishima and Honda discovered the photocatalytic water splitting phenomenon on a TiO_2 single crystal under UV light irradiation [27]. TiO_2 has been quickly attracted intensive research interests for various applications, involving in the fields of photovoltaic [28], hydrogen generation [29], photocatalysts [30], lithium-ion batteries [31], supercapacitors [32], fuel cells [33], pollutants degradation [34], gas sensors [35], and biomedical devices [36]. These applications not only depend on its earth-abundance, nontoxicity, and high stability, but also rely on its optical, electronic, structural, morphological, and surface properties as well as size, crystallinity, and surface facets [37]. Although TiO_2 possessed such promising properties, its white color, relatively poor conductivity, and wide bandgap (rutile of 3.0 eV, anatase of 3.2 eV, and brookite of 3.4 eV) are main limitations for its practical applications [38-40]. The bandgap of rutile is relatively narrow, but the anatase is favorable because of its higher reduction potential and slower electron-hole pairs recombination rate [41]. Figure 1-2 shows the typical crystal structures of TiO_2 materials in nature and their bandgaps.
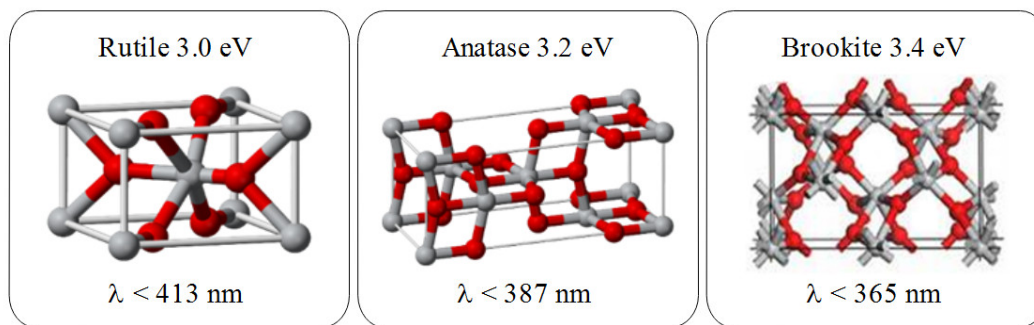
Figure 1-2 Typical crystal structures of TiO_2 materials in nature and their bandgaps.

To overcome these limitations, researchers have devoted tons of efforts on the studies of synthesis, characterization, and theoretical investigations of TiO$_2$ nanomaterials. These studies are summarized as two categories: bandgap engineering and morphology control engineering [42-44]. Bandgap engineering includes: (i) introducing non-metal elements (F, N, C, S, P, B, I, etc.) [45-48] or metal ions (V, Cr, Mn, Fe, Ni ions) [49-52] into TiO$_2$ crystalline lattices, (ii) incorporation of metal elements (Pt, Au, Ag, Rh, Ru, etc.) [53-55] or semiconductors (PbS, Cu$_2$O, CdS, ZnS, MoS$_2$, InP, CdTe, etc.) [56-60] onto TiO$_2$ surface, and (iii) phase transition or vacancies formation into TiO$_2$ crystal structure [61]. In principle, bandgap engineering on TiO$_2$ is a crucial process for narrowing bandgap, enhancing solar light harvesting, improving carrier separation, and suppressing carrier recombination.
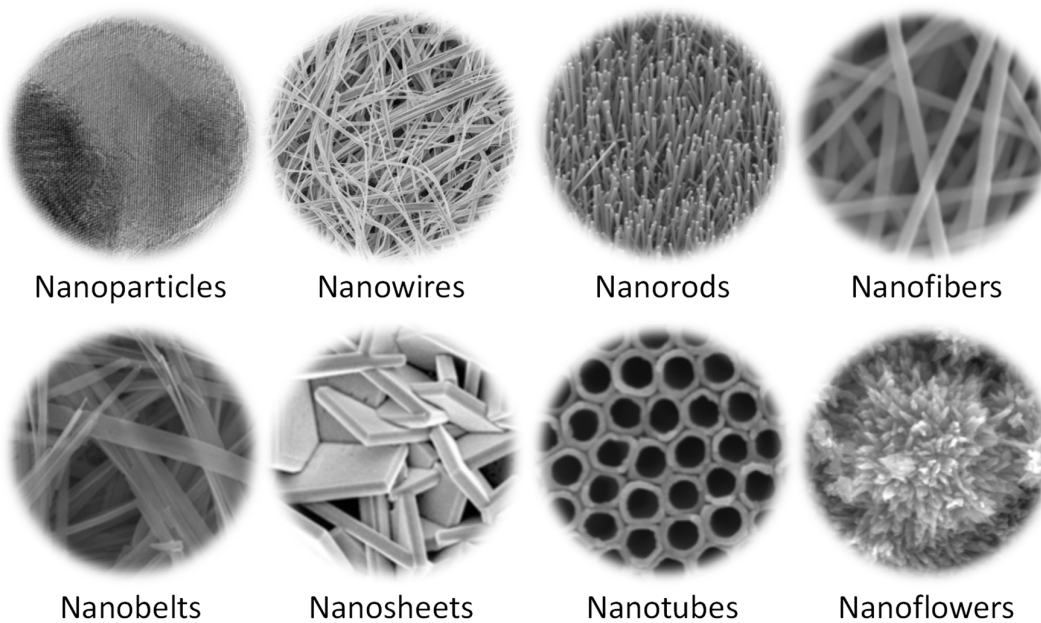
Figure 1-3 TiO$_2$ nanomaterials in different morphologies.

Morphology control engineering is to synthesize TiO$_2$ materials in a diversity of nanostructures, such as nanoparticle [62], nanowire [63], nanorod [64], nanofiber [65], nanobelt [66], nanotube [67-70], nanosheet [71], nanoflower [72], etc, as shown in Figure 1-3. As the feature size down to the nanometer, TiO$_2$ nanomaterials can offer great surface-active sites because of their quite large surface-to-volume ratio. These

surface-active sites can act as the redox centers to accelerate the reaction between TiO_2 and the interacting media [73]. Compared with bulk materials, the nanocrystallized TiO_2 materials can improve their chemical activity, phase-transition pressure, solubility, as well as melting point [74]. Therefore, the performance of TiO_2-based devices or systems could be further improved by the development of appropriate nanostructures with well-engineered composition, geometry, crystallography, and integration. In this thesis, TiO_2 nanotubes has selected as the main functional material due to its several advantages: (1) well-aligned nanotubular structure provides a light-trapping well for light harvesting, a specific path for charge transporting, a straight channel for electrolyte filling and ions transporting, and a capsule-shaped cavity for reactants adsorbing; (2) higher specific area offers a larger TiO_2/electrolyte interface or TiO_2/gas reaction site; (3) excellent mechanical strength ensures TiO_2-based devices and systems` stability and reliability.

1.3 Mechanisms of Photo-energy Conversion
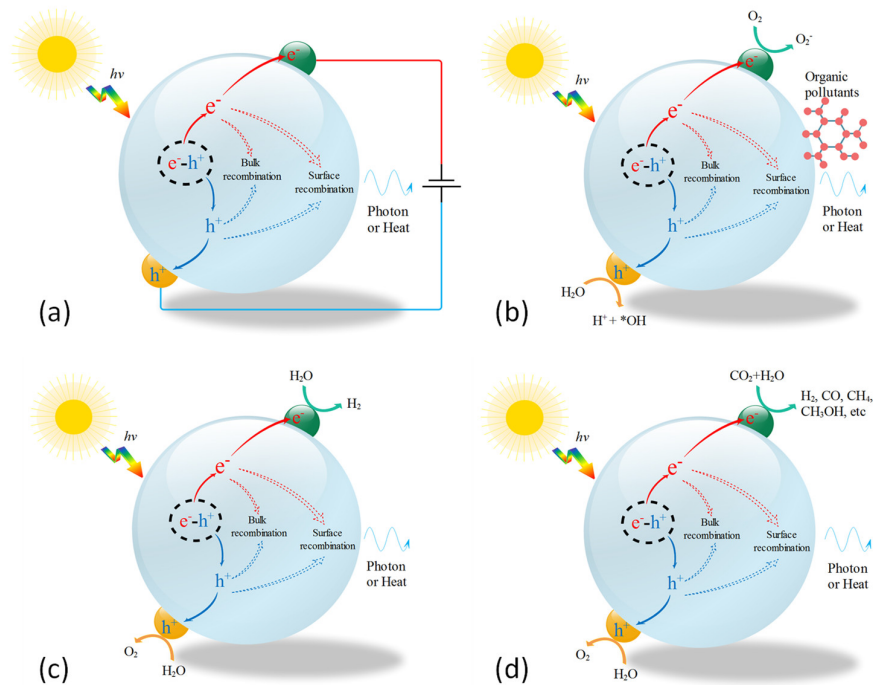
Figure 1-4 Illustration of several typical applications in the photo-energy conversion, (a) photovoltaics, (b) degradation, (c) photocatalytic water-splitting, and (d) photocatalytic CO_2 conversion.

Although TiO$_2$ nanotubes have been used as the primary functional material in the field of solar utilization (such as DSSCs [75], photocatalytic water splitting [76], photocatalytic CO$_2$ conversion [77], and photo-degradation [78], etc.), the involved fundamental mechanisms for energy conversion are similar. Figure 1-4 illustrates the photo-energy conversion processes involved in photovoltaics, degradation, photocatalytic hydrogen generation, and CO$_2$ conversion. A typical photo-energy conversion process consists of several steps: light absorption, excited charges (electrons and holes) generation, excited charges separation, excited charges transport, and excited charges recombination [79]. One more step of a redox reaction is involved in photocatalytic water splitting and photocatalytic CO$_2$ conversion. These processes affect the final yields of electricity, hydrogen, or solar fuels.

(1) Light absorption

TiO$_2$ nanomaterials act as the light harvesters to absorb as much light as possible, instead of reflecting or scattering of light. Primarily, the ability to absorb sunlight of photocatalysts depends on their natural colors [80]. For example, "white" reflects all colors while "black" absorb all colors so that no light is reflected or scattered. TiO$_2$ nanomaterials almost reflect all colors in visible regime owing to their white color. Therefore, blackening treatment of TiO$_2$ nanomaterials is a necessary approach to enhance the absorption in visible spectrum [81]. Also, the absorption ability relies on the surface morphologies of material, such as "black silicon" with a needle-shaped surface shows high absorption in visible light [82]. Similarly, tubular structure of TiO$_2$ nanotubes also provides light-trapping wells for solar light harvesting.

(2) Excited charges generation

After absorbing sunlight, TiO$_2$ nanomaterials should have high efficiency to capture the photons with the energy equals to or exceeds its bandgap energy and then generate excited charge carriers, as shown in Equation (1). For the anatase phase of 3.2 eV, TiO$_2$ nanomaterial can only capture the energy of photons with the wavelength less than ~387 nm [83]. To increase the number of photo-excited charge carriers, narrowing bandgap energy of TiO$_2$ nanomaterial is a crucial strategy by bandgap engineering [84].

6

$$E_{photon} = \frac{1240}{\lambda\,(nm)} >= E_g \tag{1}$$

$$Photocatalysts \xrightarrow{hv} e^- + h^+ \tag{2}$$
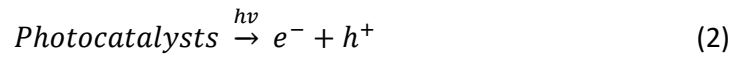
where, E_{photon} is the photon energy, λ is the wavelength of absorbed light, E_g is the bandgap energy of TiO₂ nanomaterial.

(3) Excited charges separation

After obtained the photon-energy, the electrons in the valence band are excited to the conduction band, while the holes are left in the valence band. Upon excitation, the fate of the separated electrons and holes can follow several pathways: transport, bulk recombination, or surface recombination [85].

(4) Excited charges transport

The separated electrons and holes may need to overcome several energy barriers and transport on the surface of TiO₂ nanomaterial ready for the subsequent chemical reactions. Efficient charges separation and rapid charges transport are significant for the final yields. Usually, the design of built-in internal electric field on TiO₂ nanomaterials is useful for charges separation and transport [86]. These built-in internal electric fields are achieved by p-n junction (TiO₂ coupled with semiconductors) [87], Schottky junction (TiO₂ contact with metals, electrons are favourable from TiO₂ to metal due to the potential difference between the metal and TiO₂) [88], phase junction (anatase-rutile phase junction) [89-90], and space charge region (doping with metal or non-metal ions) [91]. Also, highly conductive materials are also beneficial to charges transport [92]. Therefore, heterojunction modification and conductivity improvement on TiO₂ nanomaterials are fundamentally crucial for charges separation and transport.

(5) Excited charges recombination

During charges transport, the most of separated electrons and holes are recombined in the bulk of TiO₂ nanomaterials before reaching to the surface owing to their intrinsic electronic and structural properties [93], as shown in Equation (3). In fact, time-resolved

spectroscopic studies reveal that ~90% of photo-generated electron-hole pairs are rapidly recombined by releasing heat or emitting fluorescence after excitation. Only ~10% separated electrons and holes could reach the surface of TiO_2 nanomaterial and involve the subsequent redox reactions [94]. As a result, the photo-energy conversion efficiency by TiO_2 nanomaterials is usually limited by the fast recombination of photogenerated electron-hole pairs. The recombination of electron-hole pairs could occur on the defects or dopants of TiO_2 nanomaterial due to lack of a driving force to separate and transport them. Therefore, efficient charge separation and transport are an effective way to suppress electron-hole recombination [95].

$$e^- + h^+ \rightarrow Heat\ or\ Photons \qquad (3)$$
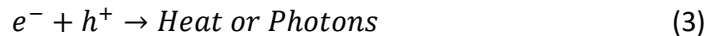
(6) Redox reaction

The electrons and holes migrated on the surface of TiO_2 nanomaterials may involve the redox reactions with adsorbed reactants (H_2O, CO_2, or other organic molecules) on reduction and oxidation centers. For photocatalytic water-splitting reaction, the electrons and holes are acted as reducing agent and oxidizing agent to produce H_2 and O_2, respectively [96]. For CO_2 conversion, the holes migrate to oxidation centers breaking water into hydrogen ions (H^+) and oxygen atoms, while the electrons reduce CO_2 with H_2O into CO, CH_4, and CH_3OH, etc. on reduction centers. Apparently, the final yields of solar fuels (H_2, CO, CH_4, CH_3OH, etc.) are mainly determined by the number of electrons and holes involved in redox reactions. Besides, the redox reactions for solar fuels yields also depend on the band-edge positions of photocatalysts [97-98]. For photocatalytic water-splitting, the match of the bandgap and band-edge positions are essential to facilitate the redox reaction of H_2O. The bottom position of the conduction band should be more negative than the reduction potential of H^+/H_2 (-0.41 V vs. NHE @ pH=7), whereas the top position of the valence band should be more positive than the oxidation potential of O_2/H_2O (+0.82 V vs. NHE @ pH=7) [99]. Similar requirements also for photocatalytic CO_2 conversion, photocatalysts capable of catalyzing CO_2 with H_2O should possess conduction band edge higher or more negative than the redox potential for CO_2 reduction, whereas the valence band edge should be lower or more positive

8

than the redox potential for the oxidation of H_2O to O_2. Table 1 is summarized the possible reactions related to photocatalytic water-splitting and CO_2 conversion [100], and Figure 1-6 shows band-edge positions of typical photocatalysts relative to the potential levels of the redox reactions involved in the water-splitting and CO_2 conversion [101-103].

Table 1 Possible reactions related to photocatalytic water-splitting and CO_2 conversion.

Reactions	E^0 (V) vs. NHE (pH=7)	Equation
$CO_2 + 2H^+ + 2e^- \rightarrow HCOOH$	-0.61	(4)
$CO_2 + 2H^+ + 2e^- \rightarrow CO + H_2O$	-0.53	(5)
$CO_2 + 4H^+ + 4e^- \rightarrow HCHO + H_2O$	-0.48	(6)
$CO_2 + 6H^+ + 6e^- \rightarrow CH_3OH + H_2O$	-0.38	(7)
$CO_2 + 8H^+ + 8e^- \rightarrow CH_4 + 2H_2O$	-0.24	(8)
$2H^+ + 2e^- \rightarrow H_2$	-0.41	(9)
$H_2O + 2h^+ \rightarrow 1/2\ O_2 + 2H^+$	+0.82	(10)
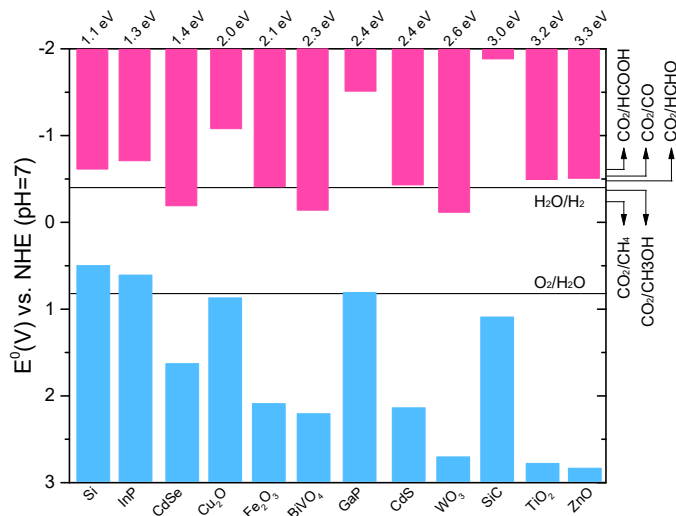
Figure 1-5 Band-edge positions of typical photocatalysts relative to the potential levels of the redox reactions involved in the water-splitting and CO_2 conversion.

Based on the mechanism analysis of photo-energy conversion, photocatalysts with excellent activities should possess enhanced absorption, efficient charge separation, fast charge transport without bulk or surface charge recombination, and narrower bandgap, as well as appropriate conduction-valence band edge positions.

1.4 Aims and Tasks

In this thesis, the primary objective is to use heterojunction engineering to synthesize TiO$_2$ nanotubes-based electrodes for the applications of energy conversion and storage. The specific tasks are listed below:

Task 1: To prepare the pristine TiO$_2$ nanotube-based electrodes by anodization method;

Task 2: Using heterojunction engineering to decorate TiO$_2$ nanotube-based electrodes for improving the performances on light absorption, charge separation and transport;

Task 3: Deploying the applications of TiO$_2$ nanotube-based electrodes in the field of environmental and energy.

1.5 Contributions of the thesis

All research tasks have been accomplished at Department of Microsystems (USN). The candidate has performed the synthesis, characterization, and measurements of TiO$_2$-based nanocomposites under the guidance of the principal supervisor. The PhD candidate carried out all data acquisition and analysis of research tasks.

The primary scientific contributions of this work are as follows:

(1) A low-cost and straightforward approach is used to synthesize PbS QDs loaded TiO$_2$ nanotubes heterojunction nanocomposites for improving absorption and photocurrent enhancement. Meanwhile, we discovered that the photocurrent enhancement on PbS QDs/TNT is related to the number of loaded PbS QDs.

(2) An approach to improve the conductivity TiO$_2$ nanotubes was created by introducing Ti^{3+} sites. The improved conductivity is beneficial to the transportation of charge carriers.

(3) The synthesis of TiN coating layer by ALD technique on TNT shows superior conductivity as comparing to the electrochemical reduction treatment through introducing Ti^{3+} sites.

(4) The synthesized "black" TNT shows the enhanced absorption in the visible regime and its photocurrent density is also increased under visible illumination compared with that of pristine TNT. Meanwhile, the discovery of photocurrent densities on CdSe QDs/Ti^{3+}/TNT is related to the size of loaded CdSe QDs.

(5) The synthesized Mo$_2$S/CdS/TNT heterojunction nanocomposites by magnetron sputter technique show the enhanced yields on the production of H$_2$, CO, and CH$_4$, which provide a promising approach for producing solar fuels.

(6) Simultaneously loading Au NPs and PbS QDs on Ti^{3+}/TiO$_2$ nanotubes is a unique technique to create efficient separation centers for fast charge separation and photocurrent enhancement.

1.6 Outline of the thesis

The thesis is organized according to the published and submitted articles. The first chapter "Introduction" presents the background and the motivation of the research. The second chapter "Summary of articles" gives the brief description and discussion of selected articles. These articles are organized systematically to show the progress of the research step by step. The third chapter "Conclusions" are summarized the contributions of this work to science.

2   Summary of Articles

In this chapter, six articles are collected to highlight the research contributions during the Ph. D period. The research is summarized as three categories: (1) investigation of single-heterojunction TiO$_2$ nanotube electrode in Article 1, Article 2, and Article 3; (2) study of double-heterojunction TiO$_2$ nanotube electrode in Article 4 and Article 5; (3) probe of multiple-heterojunction TiO$_2$ nanotube electrode in Article 6. Collected articles are briefly described based on the research motivation, experiments, results and discussion, and conclusions. The collected articles are organized regarding the research category rather than the publication date. The full-length articles are enclosed at the end of the thesis.

2.1 Single-heterojunction TiO$_2$ nanotube electrode

In this section, three distinct single-heterojunctions are formed on TiO$_2$ nanotube electrodes by different materials, such as PbS quantum dots, Ti^{3+} sites, and TiN.

2.1.1 PbS Quantum dots/TiO$_2$ heterojunction (Article 1)

Motivation

The motivation of this work is based on the illustration of photo-energy conversion in Section 1.3. Absorption of sunlight is the prerequisite for TiO$_2$ materials. Also, the photocatalysts should have high efficiency in generating excited charges after absorbing light. However, TiO$_2$ nanotubes with the bandgap of 3.2 eV only absorb UV irradiation (< 387 nm, accounting for 4~5% of solar spectrum) [104]. Loading semiconductors with narrower bandgap on TiO$_2$ nanotubes extends their absorption into the visible regime. PbS QDs are a nano-sized semiconductor (diameter of 1~10 nm) [105] and considered as efficient light harvestors to improve light absorption in the solar spectrum.

Experiments

TNT-based electrodes were fabricated by anodization of Ti foil in a fluoride-containing electrolyte [106]. Then, the pristine TNT electrodes were annealed at 500 ˚C for 5 hours

to form anatase phase. Commercially available lead sulfide (PbS) core-type QDs were purchased from Sigma-Aldrich for preparing PbS QDs solutions. PbS QDs were loaded on TNT electrodes by the ultrasonic-assisted dip-coating process. PbS QDs/TNT heterojunction electrodes were formed after ethanol volatilizing. The schematic process flow for fabrication of TNT electrode decorated with PbS QDs is shown in Figure 2-1.
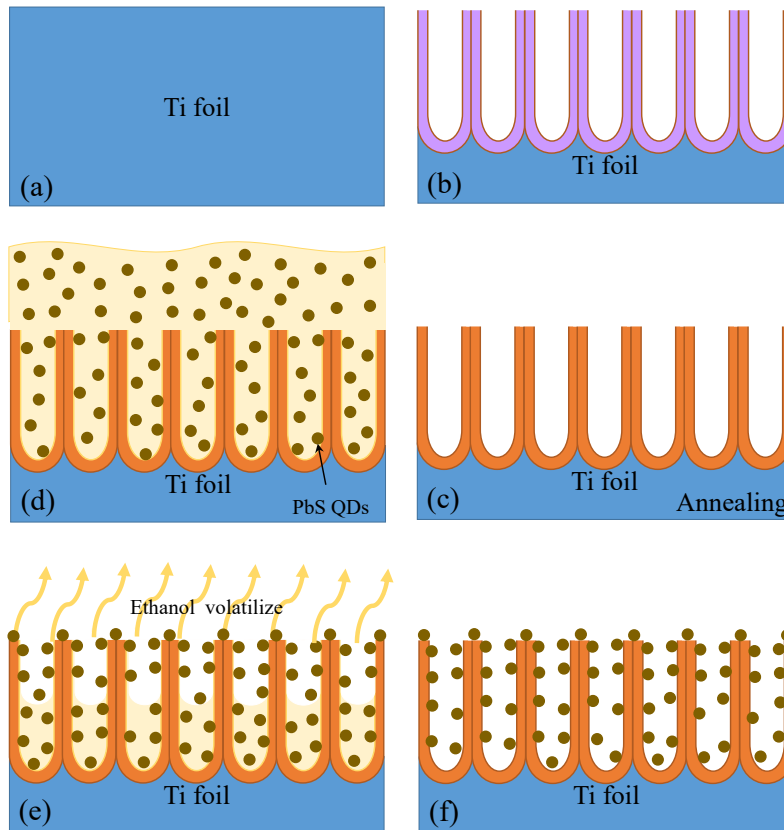
Figure 2-1 Schematic process flow for fabrication of TiO₂ nanotubes electrode decorated with PbS QDs, (a) cleaning Ti foil, (b) anodization, (c) annealing, (d) dip-coating by PbS QDs solution, (e) ethanol volatilization, and (f) PbS QDs/TiO₂ nanotubes electrode.

Results and discussion

Figure 2-2 shows the top-view SEM images of TNT and TNT loaded with PbS QDs. TNT is highly ordered with an average diameter of ~ 150 nm and average tube thickness of ~

20 nm. The mono-dispersed QDs with the size of ~30 nm are formed clusters and anchored on the TNT`s opening orifices or the gap between two TNTs.
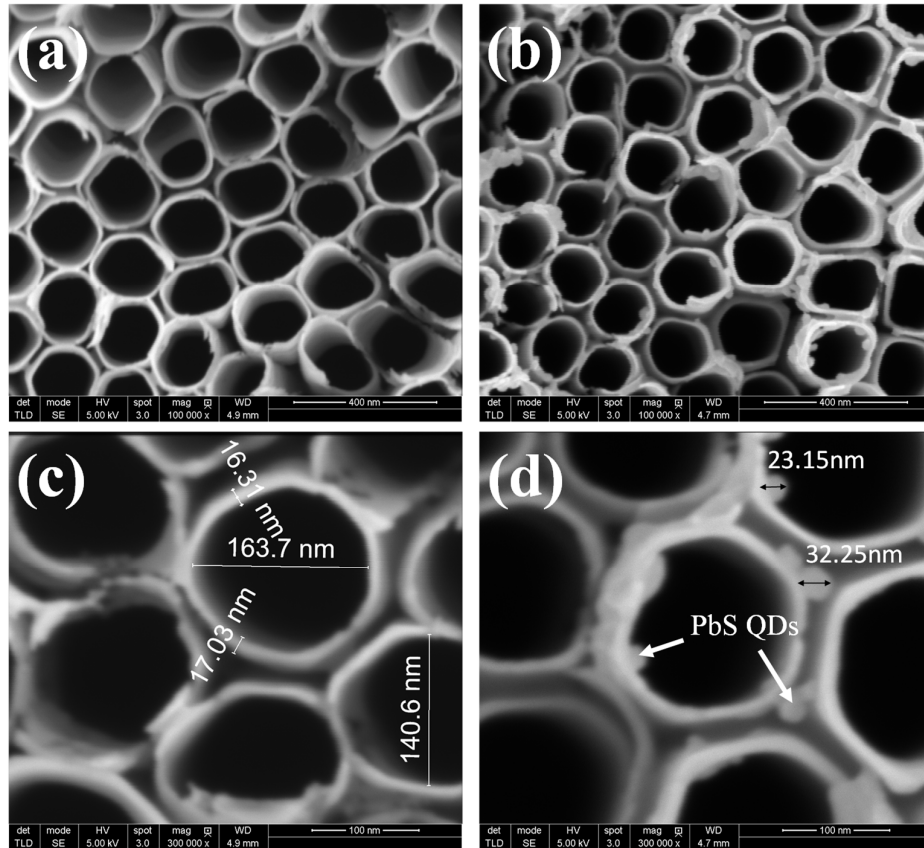
Figure 2-2 (a) SEM images of TNT, (b) TNT loaded with PbS QDs, (c) magnification image of TNT, and (d) PbS QDs.

Figure 2-3 (a) shows the UV-vis absorption spectra of pristine TNT, TNT/PbS-1, TNT/PbS-2 and TNT/PbS-3. Pristine TNT presents a weak absorption of visible light at the wavelength above ~400 nm. After loading PbS QDs, the nanocomposites TNT/PbS-1, TNT/PbS-2, and TNT/PbS-3 show enhancement in visible regime from 400 nm to 800 nm. Interestingly, TNT loaded with PbS QDs present the weakening in UV light at the wavelength lower than ~ 360 nm, even though PbS QDs allow panchromatic utilization of solar spectrum from UV to near infrared spectrum (NIR). Figure 2-3 (b) shows I-V characteristics of pristine TNT, TNT/PbS-1, TNT/PbS-2 and TNT/PbS-3 under UV illumination with the light intensity of 880 mW/cm². The inset image of Figure 2-3 (b) is

the schematic setup for the measurements of TNT/PbS QDs electrodes. Compared with pristine TNT, the photocurrents of TNT/PbS-1, TNT/PbS-2, and TNT/PbS-3 are obviously enhanced in both forward and reverse bias potential. For example, the photocurrent of TNT/PbS-3 is ~65.7 times of pristine TNT at the forward bias potential of +4 V, whereas ~5 times of that at a reverse bias potential of -4 V.
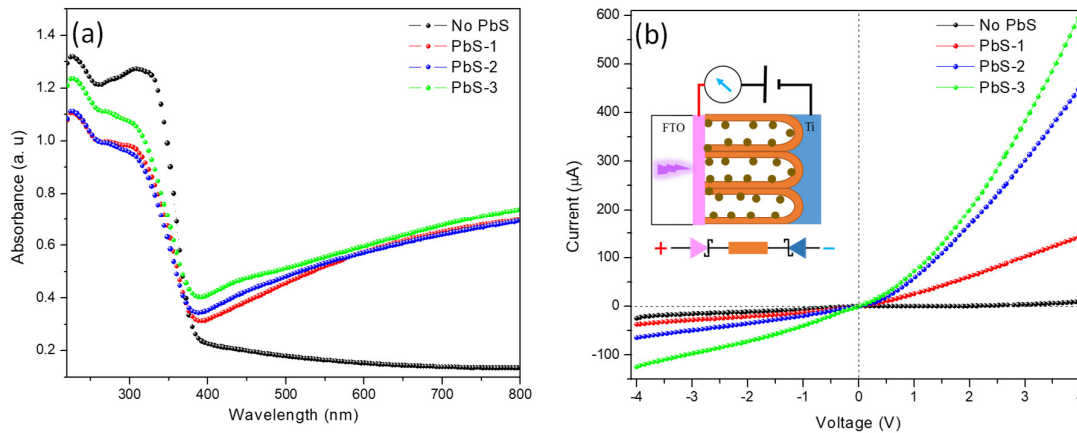
Figure 2-3 (a) UV-vis absorption spectra of pristine TNT, TNT/PbS-1, TNT/PbS-2 and TNT/PbS-3, (b) I-V characteristics of pristine TNT, TNT/PbS-1, TNT/PbS-2 and TNT/PbS-3 under UV illumination with the intensity of 880 mW/cm^2.

The physical structure of TNT electrode is considered as metal/semiconductor/metal double Schottky barrier diodes [107]. The equilibrium state of pristine TNT is shown in Figure 2-4 (a). Under UV illumination, photo-generated electrons in the conduction band of TiO$_2$ flow into FTO glass to form positive current or flow into Ti foil to create a negative current. The barrier height on the Ti foil interface ($q\Phi_T$) at the forwarding bias is much smaller than that on FTO ($q\Phi_F$) interface at the reverse bias. The number of electrons flowing into FTO (positive current) is much more significant than that flowing into Ti foil (negative current) under the built-in electric field. In PbS QDs/TNT heterojunction electrode, its band diagram is combined with the bandgap of PbS QDs, as the shown in Figure 2-4 (b). Under UV illumination, the electrons are transferred from the conduction band of PbS QDs to the conduction band of TNT, whereas the holes on valence band of PbS QDs are cascaded down to TNT. The extra electron-hole pairs contributed by PbS QDs result in the photocurrent enhancement during UV illumination.

16
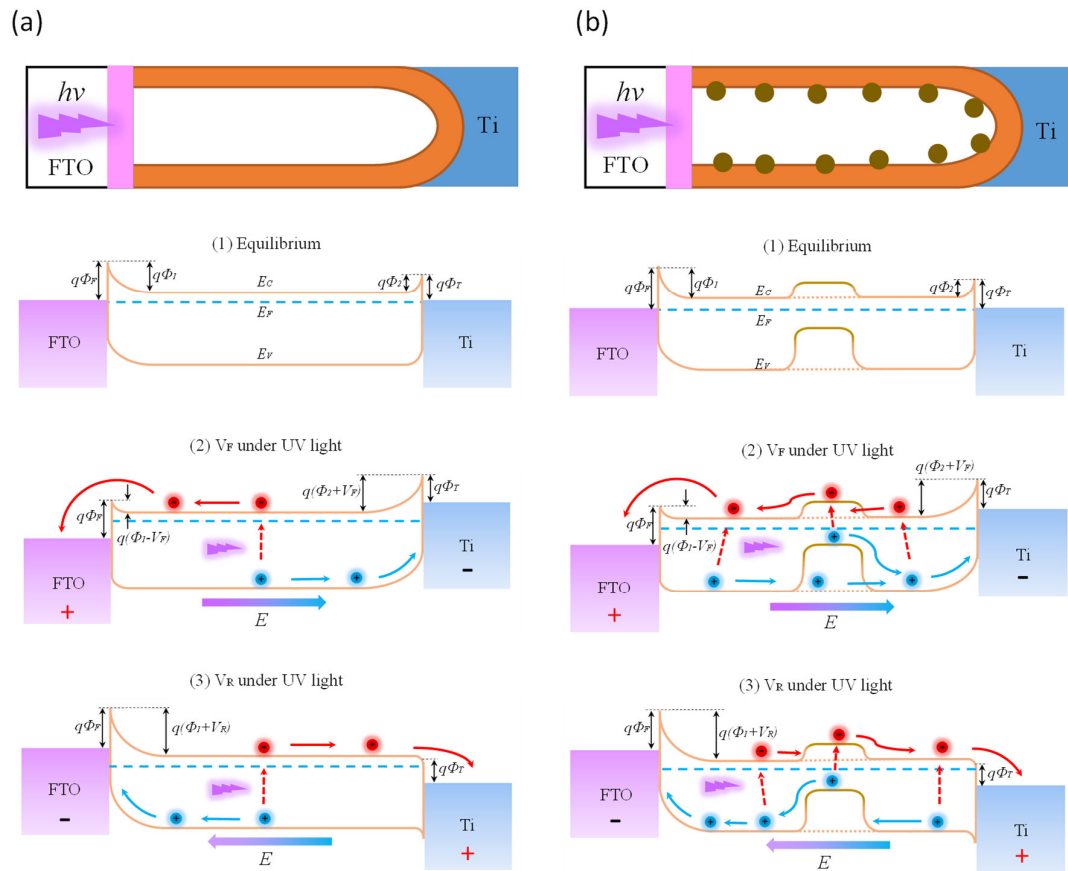
Figure 2-4 (a) Band diagram of TNT without PbS QDs and (b) PbS QDs/TNT in the equilibrium state without UV illumination, in forwarding bias potential and reverse bias potential under UV illumination.

Conclusions

TNT decorated with nearly-disperse oleic acid (OA) capped PbS QDs/clusters have been synthesized by the ultrasonic-assisted dip-coating process. The formed PbS QDs/TNT heterojunction electrodes show obvious photocurrent enhancement under UV illumination. The enhanced I-V properties are well explained by the contribution of extra electron-hole pairs generated on PbS QDs. Although these PbS QDs/TNT heterojunction electrodes were systematically investigated under UV irradiation, these electrodes also show promising applications in the visible regime, such as solar cells, photodetectors, and photocatalysts.

2.1.2 Ti^{3+} sites/TiO$_2$ heterojunction (Article 2)

Motivation

TiO$_2$ nanomaterials have been used as photoelectrodes for generating electricity, such as dye-sensitized solar cells (DSSC) [108] and perovskite solar cells [109]. The generated electricity is direct to use or store in batteries. If TiO$_2$ nanotubes are used as the electrode material for supercapacitors or lithium-ion battery, the energy systems (electricity generation and storage) will be easy to integrate with the same material. The motivation of this work is that the ordered TiO$_2$ tubular structures do offer large specific area, which might be used as the electrode material of supercapacitors [110]. However, the poor conductivity of TiO$_2$ nanotubes limits their capacitances [111]. To deal with this drawback, researchers have developed several approaches for enhancing the conductivity of pristine TiO$_2$ nanotubes. Among them, the electrochemical cathodic reduction is an effective technique because of simple in equipment, low in cost and easy to operate.

Another motivation of this work is that the anodized TNT are covered by a layer of "nano grass" and its formation is described by bamboo-splitting model [112]. Usually, this "nano grass" layer should be removed for getting better performance in photoelectric devices [113]. However, the appropriate retention of "nano grass" on TNT-based electrode might be beneficial to enhance capacitance for supercapacitor electrode.

Experiments

TNT electrodes were fabricated by anodization of Ti foil in a fluoride-containing electrolyte. After anodization, TNT with the surface debris of "nano grass" were rinsed with absolute ethanol in an ultrasonic bath to strip "nano grass" into different surface morphologies. Then, as-prepared electrodes were annealed at 500 ˚C for 3 hours to obtain anatase phase. Afterward, the electrodes were treated by cathodic reduction with the potential of +5 V for 15 seconds. These electrodes were denoted as "B-TNT-N" ("B" is black and "N" is the striping time), and corresponding pristine electrodes were prepared as the comparison electrodes ("B-TNT-N", "W" is white for short). Figure 2-5

shows the synthesis process for Ti^{3+} sites/TiO$_2$ heterojunction electrode via anodization technique and electrochemical reduction.
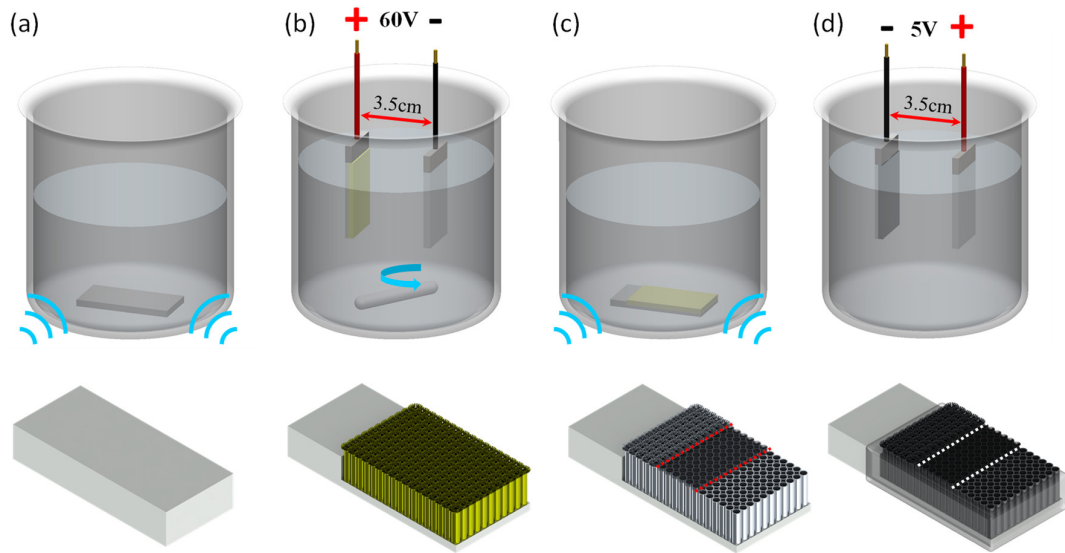
Figure 2-5 Synthesis process for Ti^{3+} sites/TiO$_2$ heterojunction electrode via anodization technique and electrochemical reduction, (a) cleaning Ti foil, (b) anodization, (c) ultrasonic striping, and (d) electrochemical reduction.

Results and discussion

Figure 2-6 shows surface morphologies of the TNT electrodes treated by ultrasonic stripping in different minutes. Pristine TNT electrode is entirely covered with "nano grass" as shown in Figure 2-6 (a). After ultrasonic treatment for 1~3 minutes in ethanol solution, parts of "nano grass" are stripped from the surface to expose the nanotubes with the diameter of ~ 140 nm, shown in Figure 2-6 (b). A large area of nanotubes is observed after ultrasonic treatment for 4~8 minutes, shown in Figure 2-6 (c). TNT begins to peel off from Ti foil after ultrasonic treatment up to ~8 minutes, exposing the "hive-like" structures on the substrate shown in Figure 2-6 (d). Therefore, the hybrid surface morphologies, both "nano grass" and nanotube, are simultaneously existed on the electrodes by controlling ultrasonic treatment in 1~7 minutes.
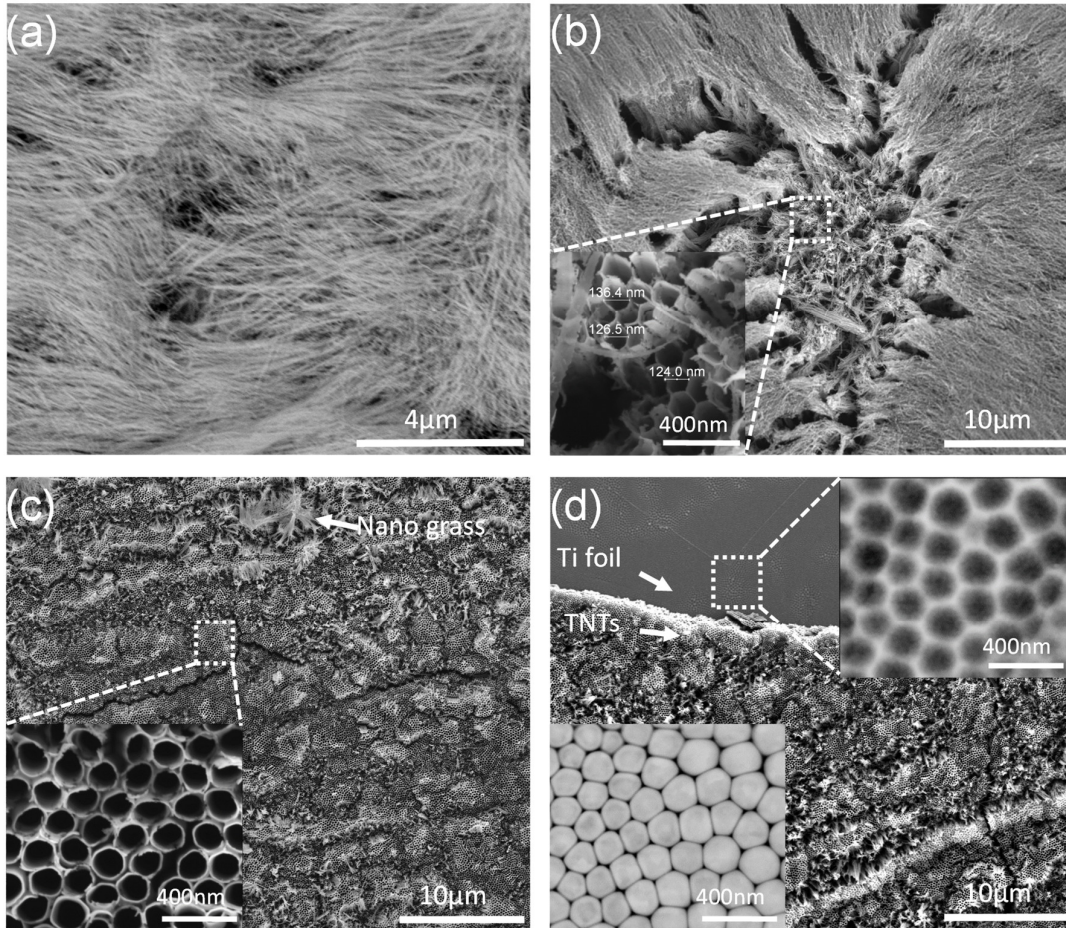
Figure 2-6 SEM images for surface morphologies of samples (a) without ultrasonic stripping, (b) with ultrasonic stripping for 1~3 mins, (c) 4~7 mins, and (d) above 8 mins.

Figure 2-7 (a) shows the Raman spectrum of W-TNT and B-TNT. Four distinct Raman peaks at 147, 395, 516, and 640 cm^{-1} from both samples can be attributed to E_g, B_{1g}, A_{1g}, and E_g modes of anatase TiO₂. E_g, B_{1g}, and A_{1g} are mainly caused by symmetric stretching vibration of O-Ti-O, the symmetric bending vibration of O-Ti-O, and anti-symmetric bending vibration of O-Ti-O, respectively [114]. Compared to that of W-TNT, Raman peaks of the B-TNT shows broadening and shifting toward a lower wavenumber, suggesting the Ti^{3+} or oxygen vacancies are introduced into B-TNT after electrochemical reduction treatment [115]. Figure 2-7 (b) shows the Nyquist plots of pristine W-TNT and B-TNT to understand the behavior of electrical conductivity and capacitive characteristics. Both W-TNT and B-TNT exhibit nearly vertical lines at the high-frequency

region. The slope of B-TNT is larger than that of W-TNT, representing B-TNT has the higher capacitance than that of W-TNT. The conductivity improvement contributes the enhanced-capacitance after introducing Ti^{3+} sites. Figure 2-7 (c) presents the CV curves of B-TNT electrodes with different ultrasonic treatment times at the scanning rate of 100 mV/s. Based on the enclosed area of CV curves, B-TNT-3 gives the maximum capacitance, which contributed to hybrid surface morphologies. Figure 2-7 (d) shows the average specific capacitance of B-TNT electrodes as a function of ultrasonic stripping times. The capacitances shown in this figure are well in accord with that in Figure 2-7 (c).
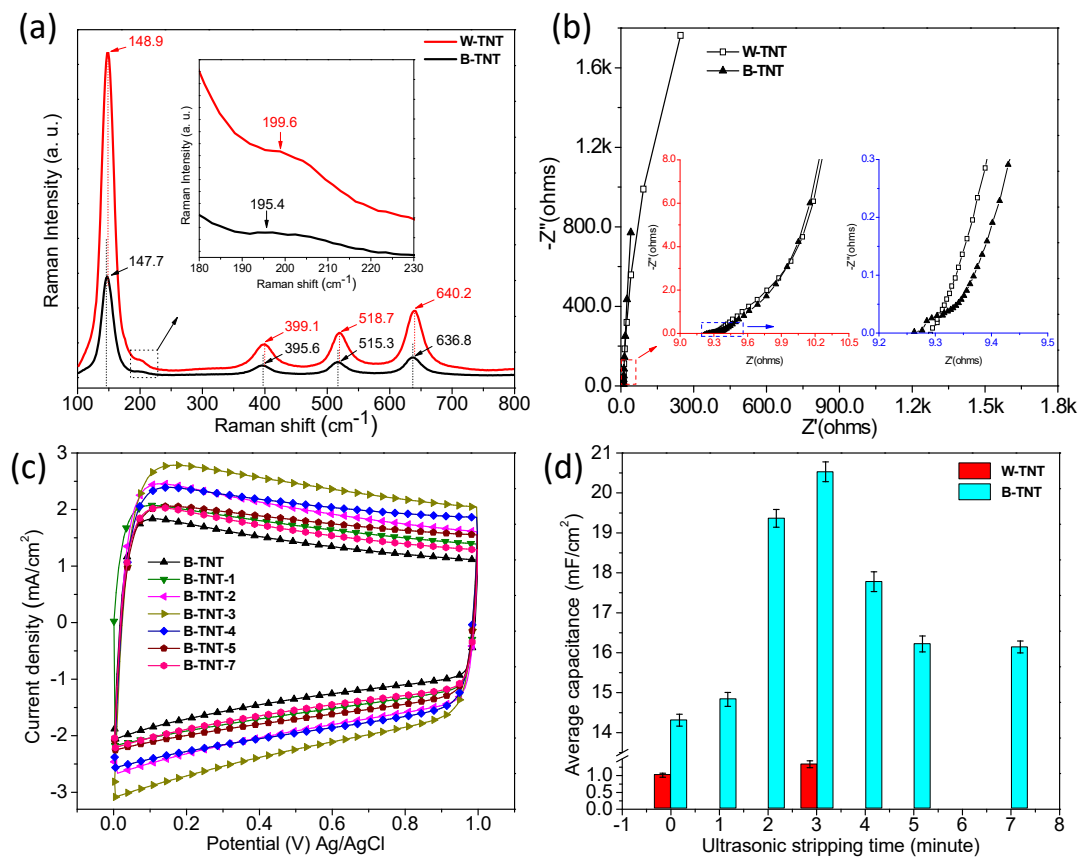
Figure 2-7 (a) Raman spectra in the range of 100-800 cm^{-1} for W-TNT and B-TNT, (b) Nyquist plots for W-TNT and B-TNT, the insets show the high-frequency regions, (c) CV curves of B-TNT with varied ultrasonic stripping time at the scanning rate of 100 mV/s, (d) Average specific capacitance of B-TNT as a function of ultrasonic stripping times.
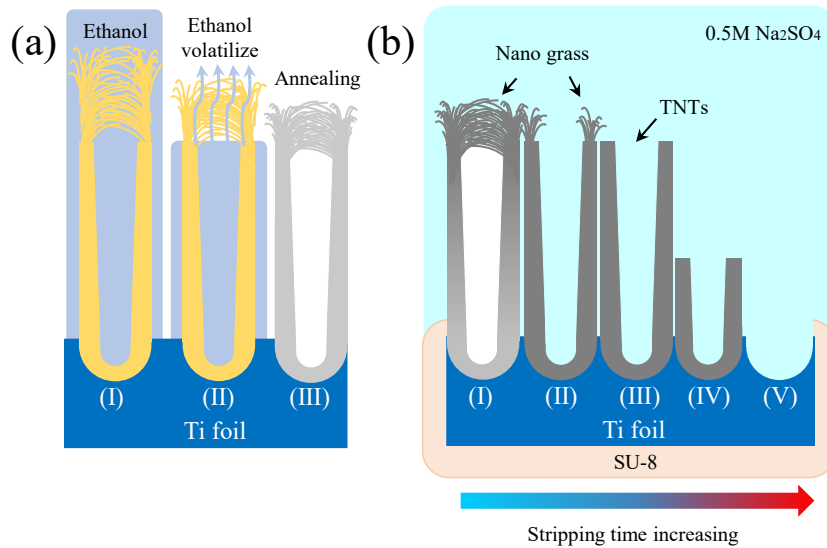
Figure 2-8 (a) Schematic of TNT with "nano grass" during cleaning and annealing processes, (b) Schematic of a cross-section of TNT in varying degrees of surface topography during electrochemical reduction and measurement.

Figure 2-8 (a) shows schematic of TNT with "nano grass" during cleaning and annealing processes. The "nano grass" is float on the top of TNT during ethanol rinsing, but they are collapsed or bundled after ethanol volatilizing. After annealing, "nano grass" are sintered together to form a dense membrane on the surface of TNT. Figure 2-8 (b) shows the TNT electrodes with different surface morphologies during electrochemical reduction and measurement. Surface morphologies of TNT electrodes are depended on ultrasonic stripping times. The more ultrasonic stripping time is performed, the less "nanograss" is retained on the surface of TNT electrodes. Overall, the capacitances are proportional to the effective surface area of hybrid nanostructures ("nano grass" and nanotubes) on electrodes.

Conclusions

Ti^{3+} sites are introduced into TiO_2 nanotubes by cathodic reduction treatment. EIS analysis indicates the conductivity of Ti^{3+} sites/TNT electrodes has been improved. Compared with pristine TNT, the capacitance of Ti^{3+} sites/TNT electrodes is increased by

14 times after introducing Ti^{3+} sites. Furthermore, the extra capacitance is contributed by appropriate retention of "nano grass" on electrodes.

2.1.3 TiN/TiO_2 heterojunction (Article 3)

Motivation

This work has been performed after the study in Article 2. The motivation of this work is to use TiO_2 nanotubes as high-performance supercapacitor electrodes. Although the capacitance of Ti^{3+} sites/TNT electrode does improve by several tens of times comparing to that of pristine TNT. The thin Ti^{3+} sites layer distributed on the very top surface of TiO_2 nanotubes is limited to enhance their capacitance [116]. Introducing high-conductive layer into TiO_2 nanotubes is a promising strategy for improving capacitance. Atomic layer deposition (ALD) is an Angstrom-level thin film deposition technique and has been used for feature size smaller than 100 nm [117]. Titanium Nitride (TiN) is a hard ceramic material [118], but it has an excellent electrical conductivity [119]. The capacitance of TNT-based electrodes might be significantly enhanced by conformal coated with a TiN layer through ALD technique.

Experiments

Before anodization, Ti foils were rinsed by acetone, isopropanol and DI water for 15 mins. TNT electrodes were fabricated by anodization of Ti foil using a fluoride-containing electrolyte at room temperature (25 ˚C). Then, pristine TNT electrodes were annealed at 500 ˚C for 3 hours to obtain anatase phase. Afterward, two approaches were applied for treating annealed electrodes: (1) Ti^{3+} sites introducing by cathodic reduction treatment under the potential of +5 V for 15 seconds; (2) conformal coating TiN layer on TNT by ALD technique. Subsequently, Ti^{3+} sites/TNT and TiN/TNT electrodes are selected to assemble as symmetric supercapacitors for the following electrochemical measurements. Figure 2-9 shows the schematic flow for fabricating Ti^{3+} sites/TNT and TiN/TNT symmetric supercapacitors.
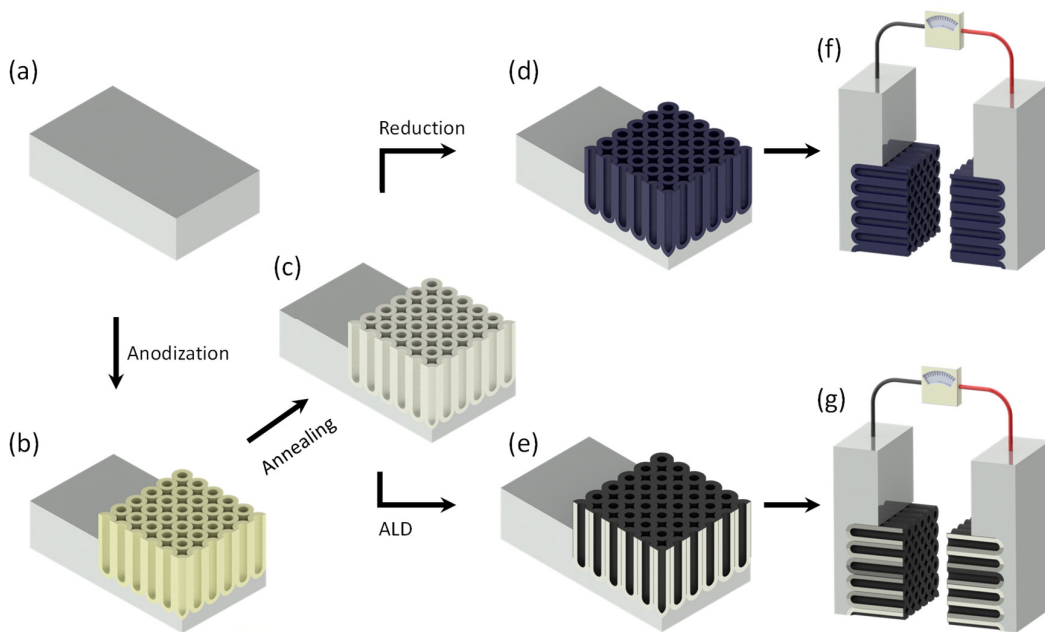
Figure 2-9 Schematic flow for fabricating Ti^{3+} sites/TNT and TiN/TNT symmetric supercapacitors, (a) cleaning Ti foil, (b) anodization, (c) annealing, (d) electrochemical reduction for introducing Ti^{3+} sites, (e) ALD for TiN/TNT electrode, (f) symmetric Ti^{3+} sites/TNT supercapacitors, (g) symmetric TiN/TNT supercapacitors.

Results and discussion

Figure 2-10 (a) shows the surface morphologies of Ti^{3+} sites/TNT electrode. The inset image of Figure 2-10 (a) indicates the nanotube diameter of ~140 nm and the tube wall thickness of ~12 nm. Figure 2-10 (b) shows SEM image of TiN/TNT electrode and its inset image presents that the nanotube diameter decreases to ~120 nm and the tube wall thickness increases to ~70 nm. Through the comparison of two parameters, the thickness of the TiN layer is estimated to be ~30 nm. Figure 2-10 (c) shows high-resolution TEM (HRTEM) image of TiN/TNT electrode and Figure 2-10 (d)~(f) shows the element of titanium, oxygen, and nitrogen by EDX mapping analysis, respectively. Figure 2-10 (g) indicates the combination of element oxygen and nitrogen, showing TiN layer is conformally coated inside and outside of TNT and the thickness of the TiN layer is ~30 nm which is in accord with the parameters as shown in Figure 2-10 (b).
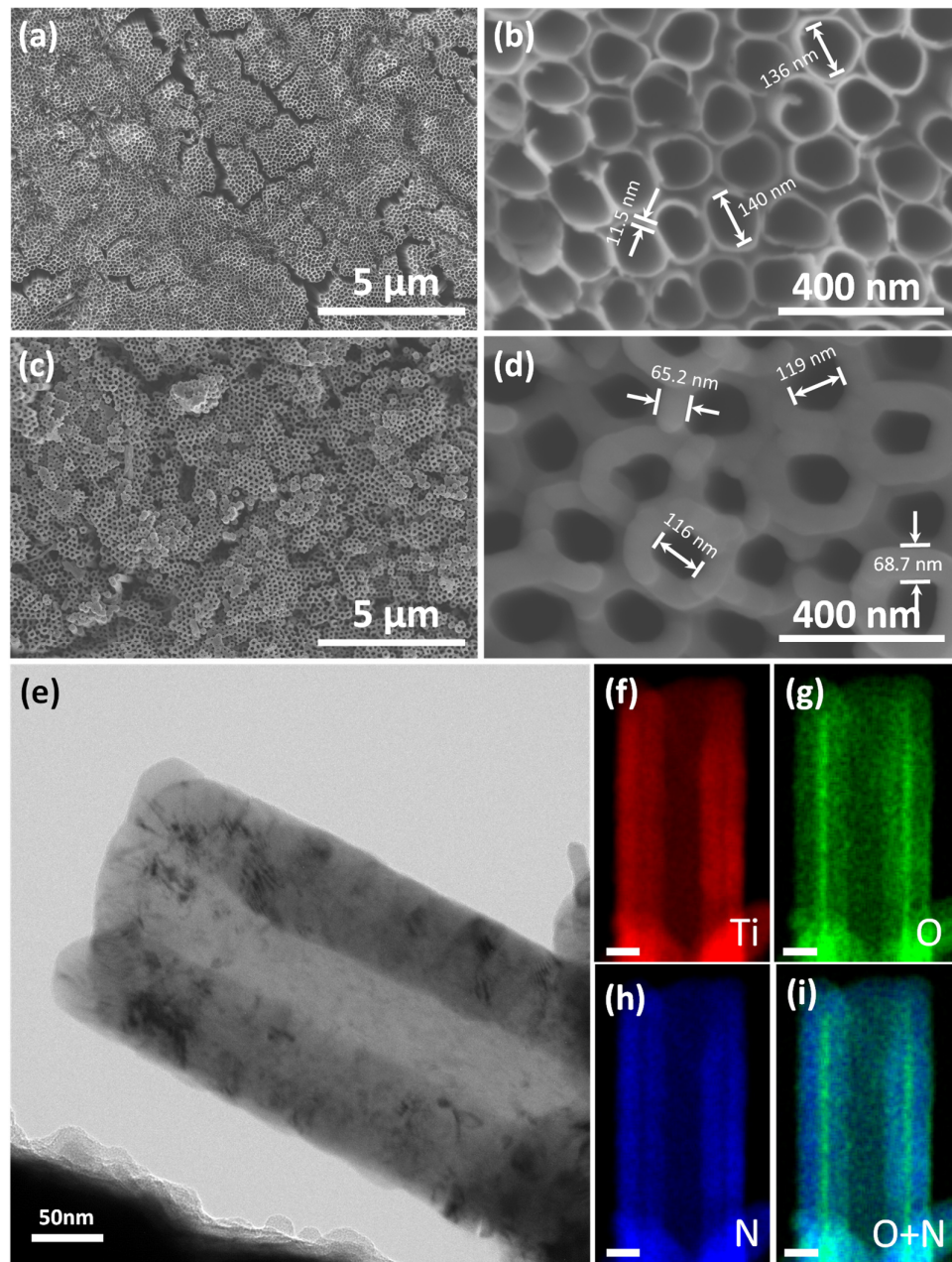
Figure 2-10 (a) SEM images of Ti^{3+} sites/TNT electrode, (b) enlarged image of Ti^{3+} sites/TNT, (c) SEM image of TiN/TNT electrode, (d) enlarged image of TiN/TNT, (e) HRTEM image of TiN/TNT electrode and scanning TEM (STEM) images, and EDX mapping of element (f) Titanium, (g) Oxygen, (h) Nitrogen, (i) Oxygen and Nitrogen.
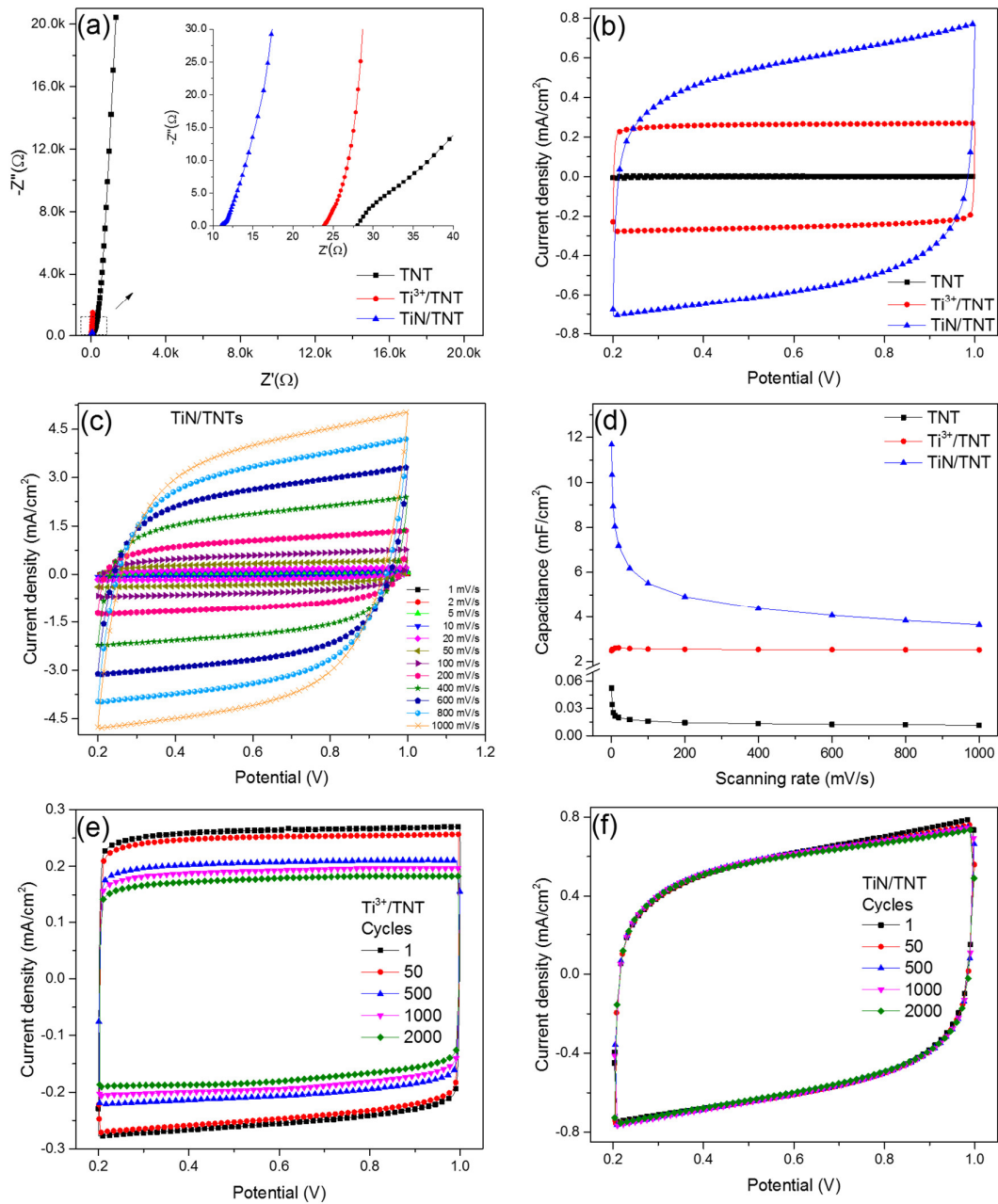
Figure 2-11 (a) Nyquist plots of TNT, Ti^{3+}/TNT and TiN/TNT symmetric electrodes, (b) CV curves of as-prepared symmetric supercapacitors at scanning rate of 100 mV/s, (c) CV curves of TiN/ TNT supercapacitors at different scanning rates, (d) calculated capacitance of as-prepared symmetric supercapacitors as the function of scanning rate, (e) CV curves of symmetric Ti^{3+}/TNT supercapacitors, and (f) TiN/TNT supercapacitors at the cycle number of 1, 50, 500, 1000, and 2000.

Figure 2-11 (a) shows Nyquist plots of TNT, Ti^{3+}/TNT, and TiN/TNT symmetric electrodes. Nyquist plots intersection on real axis indicates that the equivalent series resistance (ESR) of TiN/TNT, Ti^{3+}/TNT and TNT are 11.33 Ω, 23.95 Ω, and 28.11 Ω, respectively. The decreased ESR of TiN/TNT electrode does demonstrate the electrical conductivity of TiN/TNT has improved after coating with TiN layer. Figure 2-11 (b) shows CV curves of as-prepared symmetric supercapacitors at a scanning rate of 100 mV/s. The larger enclosed area of CV curve implies that TiN/TNT supercapacitors have the larger capacitance. Figure 2-11 (c) shows CV curves of TiN/TNT symmetric supercapacitors at different scanning rates from 1 mV/s to 1 V/s. CV curves retain a series of "quasi-rectangle" at different scanning rates, indicating excellent capacitive behavior and high rate capability. Figure 2-11 (d) shows the calculated capacitance under different scanning rate. The capacitance of symmetry TiN/TNT supercapacitors is 11.68 mF/cm^2 at the scanning rate of 1 mV/s, which is 224.6 times (0.052 mF/cm^2) and 4.7 times (2.49 mF/cm^2) than that of TNT and Ti^{3+}/TNT. The CV curves of Ti^{3+}/TNT and TiN/TNT supercapacitors at the cycle number of 1, 50, 500, 1000, and 2000 are shown in Figures 2-11 (e) and (f). The enclosed areas of CV curves are obviously decreased for Ti^{3+}/TNT but almost overlapped for TiN/ TNT supercapacitors after 2000 cycles. This data is further demonstrated that TiN/ TNT supercapacitors have excellent stability.
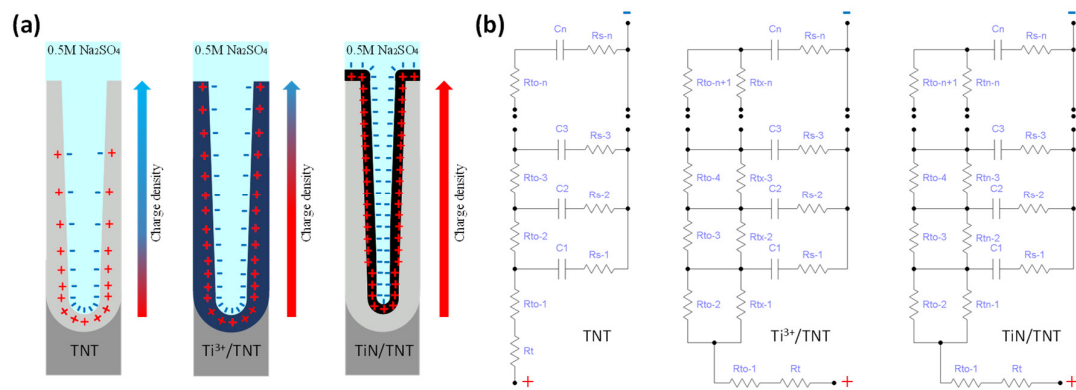
Figure 2-12 (a) Schematic diagram of TNT, Ti^{3+}/TNT, and TiN/TNT half-electrode during test, (b) ladder network equivalent circuits of TNT, Ti^{3+}/TNT and TiN/TNT half electrodes.

Figure 2-12 (a) shows a schematic diagram of TNT, Ti^{3+}/TNT and TiN/TNT half electrodes during the test. Based on the idea of finite element method, an electric double-layer capacitor (EDLC) could be equivalent to ladder network circuits [120], shown in Figure 2-12 (b). For pristine TNT electrode, the charges are mainly accumulated on the bottom of nanotubes due to the intrinsic resistance of TiO$_2$ material are large. Therefore, only a relatively small active specific area is involved in TNT supercapacitors. For Ti^{3+}/TNT and TiN/TNT electrode, the introduced Ti^{3+} sites and coated TiN layer have improved the conductivity of TNT. However, Ti^{3+} sites layer (several nanometers) is distributed on the very top surface of TNT whereas the thickness of the TiN layer can be reached up to ~30 nm. Therefore, the activated specific area for TiN/TNT is larger than that of Ti^{3+}/TNT.

Conclusions

TiN layer is conformally deposited on TiO$_2$ nanotubes by ALD technique. The TiN/TNT electrode presents the capacitance of 11.68 mF/cm^2 at a scanning rate of 1 mV/s, which is 224.6 times and 4.7 times higher than that of TNT and Ti^{3+}/TNT. Furthermore, the TiN/TNT supercapacitors present outstanding cycling stability with 98.5% retention of original specific capacitance after 2000 cycles.

2.2 Double-heterojunction TiO$_2$ nanotube electrode

2.2.1 Ti^{3+}/CdSe quantum dots/TiO$_2$ heterojunction (Article 4)

Motivation

This work is conducted after the study in Article 2. Ti^{3+} sites introduced TNT electrode presents a good conductivity which is useful for carrier transport. Besides, Ti^{3+}/TNT electrode shows a black or dark blue color which is beneficial to absorb light in visible regime [121]. The motivation of this work is to study the photocurrent properties of "black" TNT. From Article 1, the photocurrent of PbS QDs/TNT electrode is enhanced by loading with the different amounts of PbS QDs. Another motivation of this work is to

investigate the photocurrent enhancement of TNT electrode by loading with different size of CdSe QDs.

Experiments

TNT-based electrodes were fabricated by anodization method in a fluoride-containing electrolyte. Then, the pristine TNT electrodes were annealed at 600 ˚C for 5 hours to form anatase phase. Afterward, TNT electrodes were treated by a cathodic reduction in 0.5 M Na_2SO_4 solution and denoted as "T-TNT". Cadmium selenide (CdSe) QDs were purchased from Sigma-Aldrich for preparing CdSe QDs solutions. Three different sizes of CdSe QDs were loaded on Ti^{3+}/TNT electrodes by the ultrasonic-assisted dip-coating process. CdSe QDs/Ti^{3+}/TNT heterojunction electrodes were formed after ethanol volatilizing and denoted as "T-TNT-CS-N" (N is the number of CdSe QDs solution). Figure 2-13 shows the schematic process flow for fabrication of TiO₂ nanotubes electrode decorated with PbS QDs.
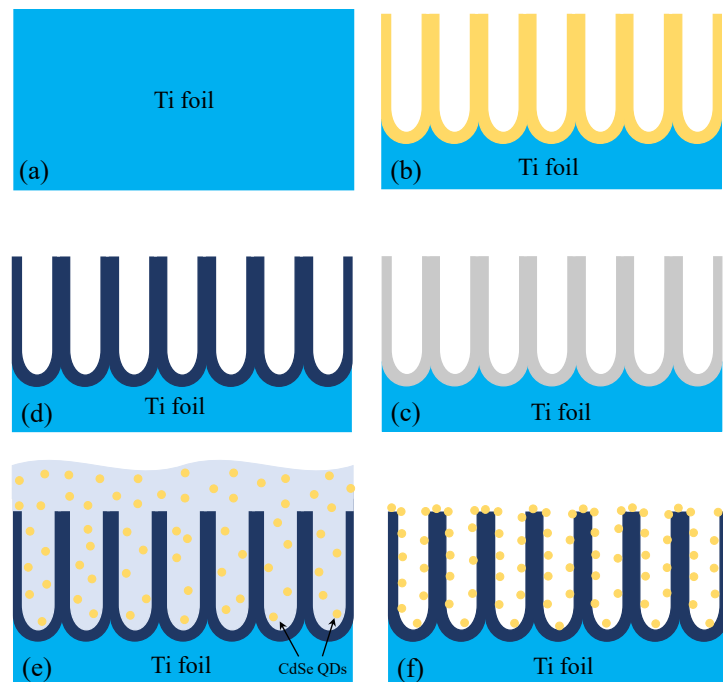
Figure 2-13 Fabrication procedures of Ti^{3+}/CdSe quantum dots/TiO₂ heterojunction electrodes, (a) cleaning Ti foil, (b) anodization, (c) annealing, (d) electrochemical

reduction, (e) loaded with CdSe QDs, (f) evaporation ethanol to form heterojunction electrodes.

Results and discussion

Figure 2-14 (a) shows surface morphologies of the pristine TNT. The average diameter and wall thickness of TNT are ~120 nm and ~18 nm. Figure 2-14 (b) shows the SEM images of Ti^{3+}/CdSe QDs/TNT electrode after loading of CdSe QDs. CdSe QDs and their clusters are naturally observed on the opening of TNT. Besides, AFM was used for characterizing the size of CdSe QDs, shown in Figure 2-14 (c) and (d). Both individual and cluster CdSe QDs are observed on scanning region. The size of individual CdSe QDs is ~20 nm which is larger than the size (2~8 nm) in literature since CdSe QDs capped with oleic acid (OA) for improving their air stability and decreasing agglomeration.
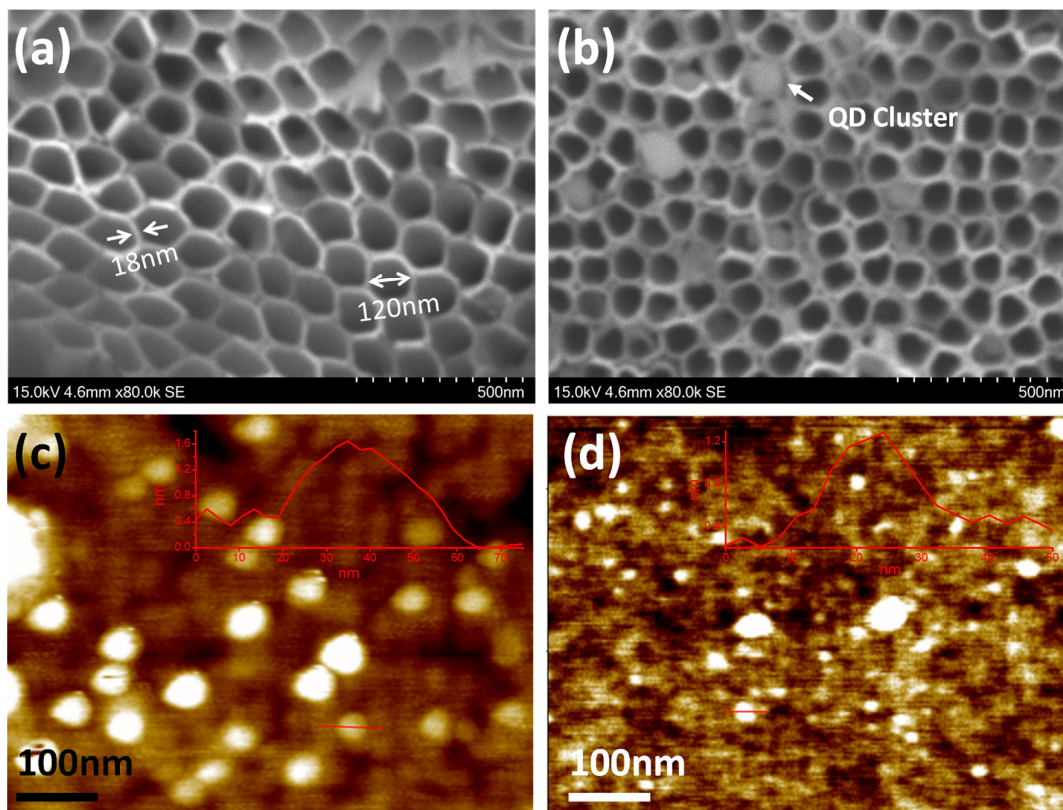
Figure 2-14 SEM images of (a) TNT, (b) TNT decorated with CdSe QDs, (c) AFM image of CdSe QDs solution-1, and (d) solution-2.
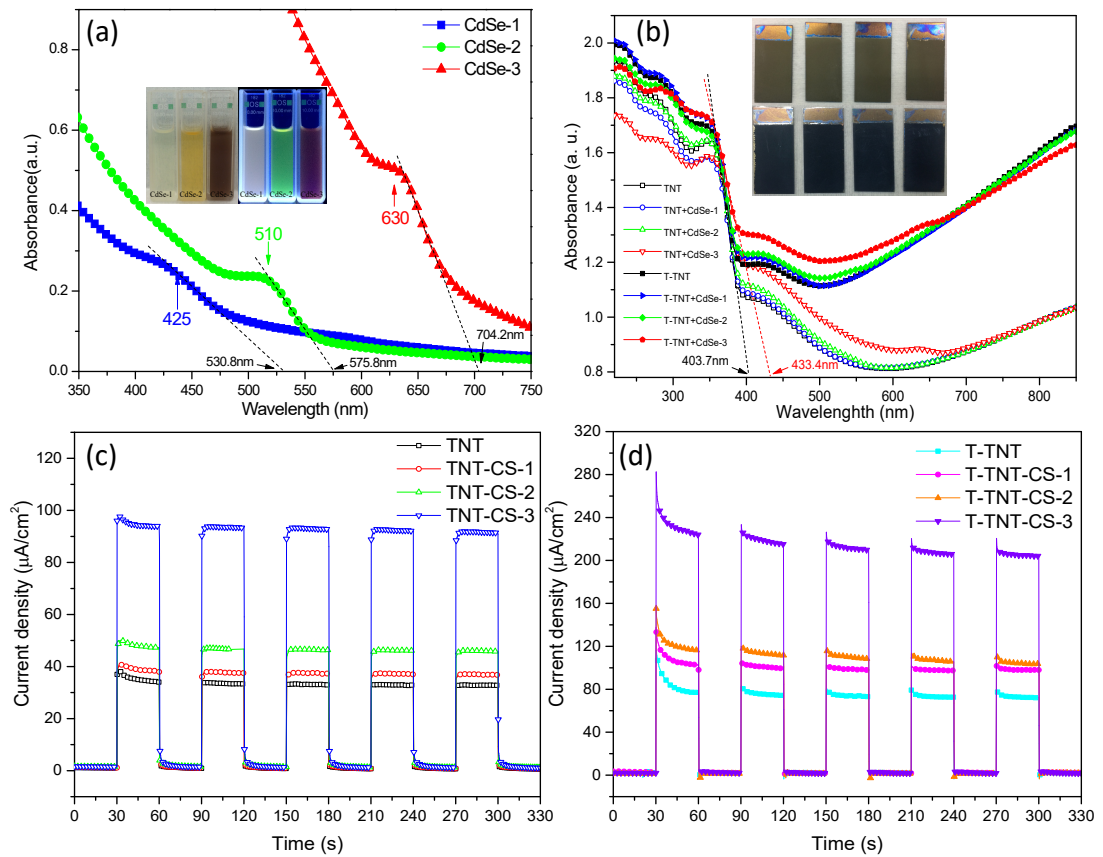
Figure 2-15 (a) absorption spectra of CdSe QD solutions, (b) UV-vis absorption spectra of as-prepared CdSe QDs/Ti^{3+}/TNT heterojunction electrodes, (c) transient photocurrent responses of (c) pristine TNT and (d) Ti^{3+}/TNT loaded with different size CdSe QDs under visible illumination at the applied potential of +1 V.

Figure 2-15 (a) shows absorption spectra of CdSe QD solutions. Three different CdSe QD solutions present the distinct peaks at 430 nm, 510 nm, and 630 nm and the intercepts at 530.8 nm, 575.8 nm and 704.2 nm for CS-1, CS-2, and CS-3, respectively. The bandgaps of CdSe QD in different sizes are calculated as 2.33 eV, 2.15 eV and 1.76 eV by E_g = 1240/λ (nm) [122]. The inset image of Figure 2-15 (a) shows the colors of as-prepared CdSe QDs solutions under natural light and UV light. Figure 2-15 (b) shows UV-vis absorption spectra of as-prepared Ti^{3+}/CdSe QDs/TiO$_2$ heterojunction electrodes Compared with pristine TNT electrodes, Ti^{3+}/TNT electrodes display enhanced absorption above ~400 nm. After decorated with CdSe QDs in a different size, the absorption of pristine TNT

and Ti^{3+}/TNT electrodes are enhanced from 400 nm to 680 nm. The inset image of Figure 2-15 (b) shows as-prepared pristine TNT and Ti^{3+}/TNT electrodes loaded with CdSe QDs. Figure 2-15 (c) and (d) show the transient photocurrent responses of pristine TNT and Ti^{3+}/TNT loaded with different size CdSe QDs under visible illumination at the applied potential of +1 V. Compared with pristine TNT (32.76 μA/cm^2), the photocurrent of Ti^{3+}/TNT (72.53 μA/cm^2) is increased by 2.2 times. Furthermore, the maximum photocurrent on the fifth pulse of CdSe QDs/Ti^{3+}/TNT is 205.17 μA/cm^2, which is 2.2 times larger than that of Ti^{3+}/TNT. Therefore, the enhanced photocurrent is contributed by both Ti^{3+} sites and CdSe QDs.
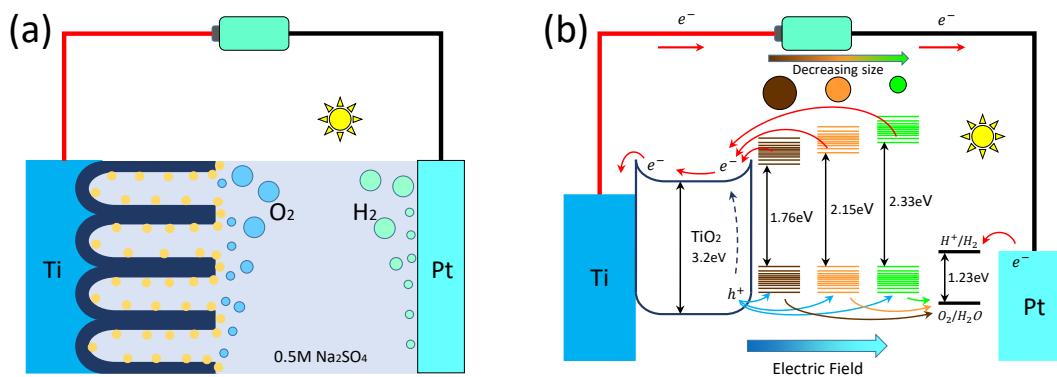
Figure 2-16 (a) schematic view of Ti^{3+}/TNT electrodes decorated with CdSe QDs during measurement, (b) band diagram of Ti^{3+}/TNT photoelectrode decorated with different size CdSe quantum dots.

Figure 2-16 (a) shows a schematic view of Ti^{3+}/TNT electrodes decorated with CdSe QDs during measurement. Under visible illumination, the electron-hole pairs are generated on CdSe QDs/Ti^{3+}/TNT electrodes and then separated by the positive bias potential applied to Ti and Pt electrodes. The water on the anode is oxidized by holes to generate hydrogen ions and oxygen (H$_2$O+2h$^+$→2H$^+$+1/2O$_2$); meanwhile, the generated hydrogen ions are combined with electrons on the cathode to produce hydrogen (2H$^+$+2e$^-$→H$_2$) [123]. Figure 2-16 (b) shows the band diagram of CdSe QDs/Ti^{3+}/TNT electrodes. The larger size CdSe QDs give the narrower bandgap (wider visible region), which is easier for generating more electron-hole pairs under visible illumination. The electrons are

jumped onto the conduction band of Ti^{3+}/TNT by the act of applied bias voltage, whereas the holes are jumped to the valence band of CdSe QDs. The separated electrons and holes are involved in photochemical water splitting reactions.

Conclusions

Ti^{3+} sites are introduced into TNT by cathodic reduction treatment. Different size CdSe QDs are loaded on Ti^{3+}/TNT electrodes by the ultrasonic-assisted dip-coating process. Photocurrent of CdSe QDs/Ti^{3+}/TNT electrodes is enhanced by several facts: (1) the color of Ti^{3+}/TNT turns to black or dark blue which is easy to absorb visible light; (2) Ti^{3+}/TNT display an excellent conductivity which is beneficial to carrier transport; (3) the loadings of CdSe QDs contribute the extra photogenerated electron-hole pairs and separation centres. This work provides an approach to synthesizing high-performance photocatalysts for water splitting.

2.2.2　MoS_2/CdS/TiO_2 heterojunction (Article 5)

Motivation

This work is conducted after the study in Article 1. PbS QDs were loaded on TNT by the dip-coating approach. After the discovery and applications of graphene-based nanosheets [124], the research on 2D transition metal disulfides has experienced rapid growth. MoS_2 is a layered material with the narrowed bandgap and can be exfoliated to single- or few-layer nanosheets [125]. Also, MoS_2 has been manifested as a potential catalyst to replace the rare and expensive noble metals (Pt, etc.) for hydrogen evolution reaction (HER) [126]. The motivation of this work is depositing metal sulfide (MoS_2 and CdS nanoparticles) by magnetron sputter technique to modify the anodized TNT electrode. Another motivation for this work is using the band-edge positions of MoS_2 and CdS to synthesize heterojunction nanocomposites for photocatalytic CO_2 conversion.

Experiments

TNT electrodes were fabricated by anodization of Ti foils. MoS$_2$ and CdS were deposited on TNT by magnetron sputter technique at different setting conditions. The photocatalytic CO$_2$ conversion tests were conducted in a gastight reactor (~ 25 mL) with a quartz plate at the top, inlet, outlet and sampling port at the bottom. A 500 W Xenon lamp was used as the illuminating source. Before photocatalytic experiments, high purity CO$_2$ was bubbled through a gas-water mixer which was heat on ~50 ˚C and then flowed into the reactor with the velocity rate of 50 sccm for 60 min to remove the residual air. The photocatalytic reaction was conducted for 5 hours. 0.5 mL of gases in the reactor was pumped out by a syringe in each hour and then injected into Gas Chromatography (GC-2010 Plus, Shimadzu) for analysis. Schematic diagram of the setup for CO$_2$ conversion measurement is shown in Figure 2-17 (a), and the physical buildup of CO$_2$ conversion system is shown in Figure 2-17 (b).
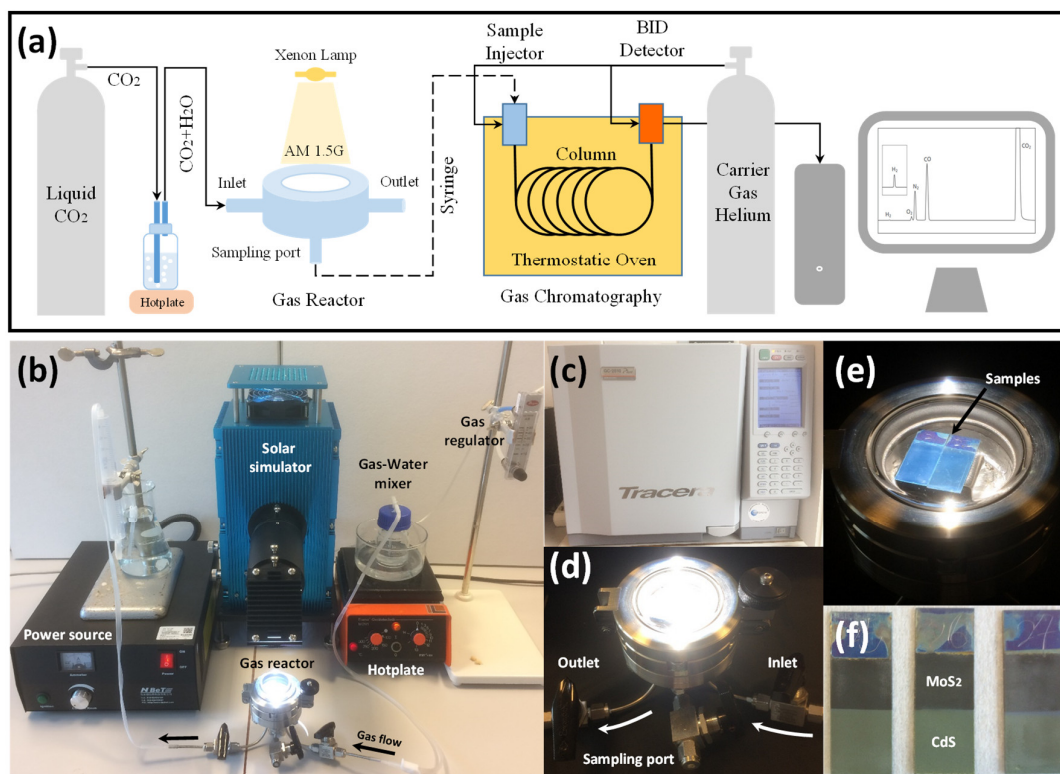
Figure 2-17 (a) schematic diagram of setup for CO$_2$ conversion measurement, (b) the physical buildup of CO$_2$ conversion system, (c) GC-2010 plus with BID detector, (d) gas

reactor under illumination with the intensity of ~100 mW/cm^2, (e) measured samples in gas reactor, (f) as-prepared TNT-MoS$_2$-CdS samples for CO_2 conversion testing.

Results and discussion
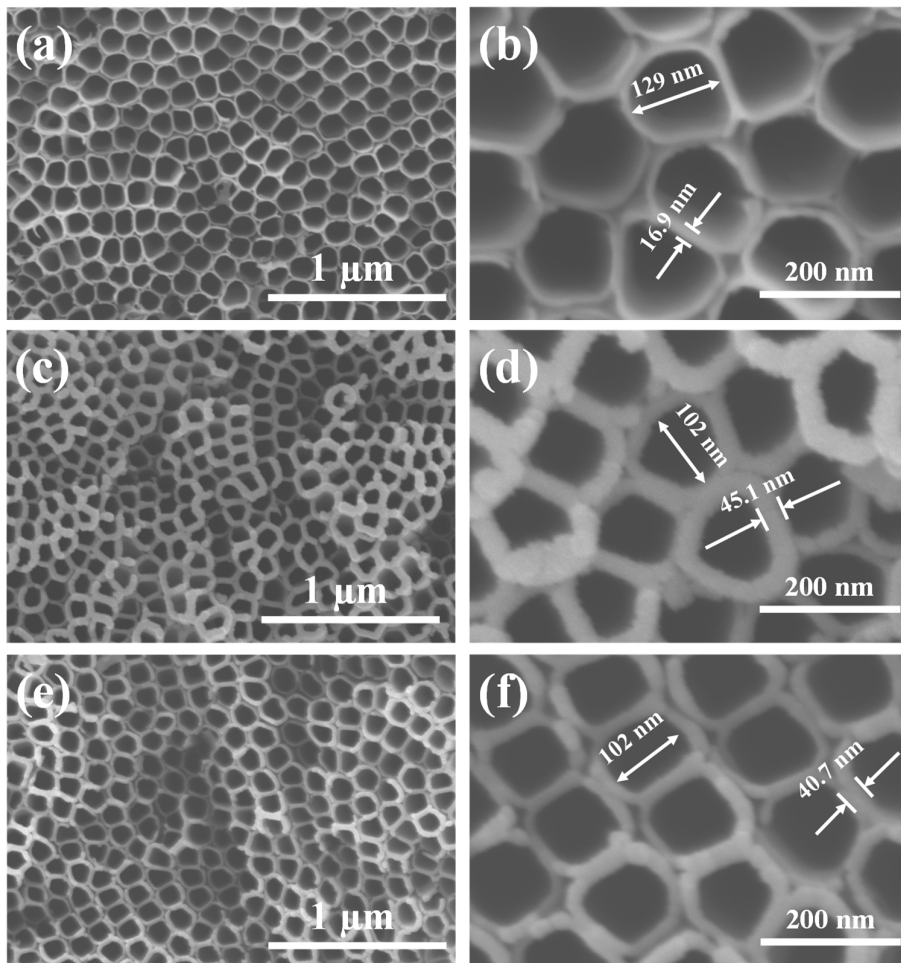
Figure 2-18 SEM images of (a) pristine TNT electrode, (b) enlarged view of TNT, (c) MoS$_2$/TNT heterojunction electrode, (d) enlarged view of MoS$_2$/TNT, (e) CdS/TNT heterojunction electrode, (f) enlarged view of MoS$_2$/TNT.

Figure 2-18 (a) and (b) show the surface morphologies of pristine TNT. The diameter and tube wall thickness of TNT are ~129 nm and ~17 nm. After deposited with MoS$_2$, the diameter shrinks to ~102 nm and the thickness of tube wall is increased to ~45 nm, shown in Figure 2-18 (c) and (d). The thickness of deposited MoS$_2$ layer could be

estimated as ~14 nm. Similarly, the deposited CdS layer is approximately ~12 nm, shown in Figure 2-18 (e) and (f).
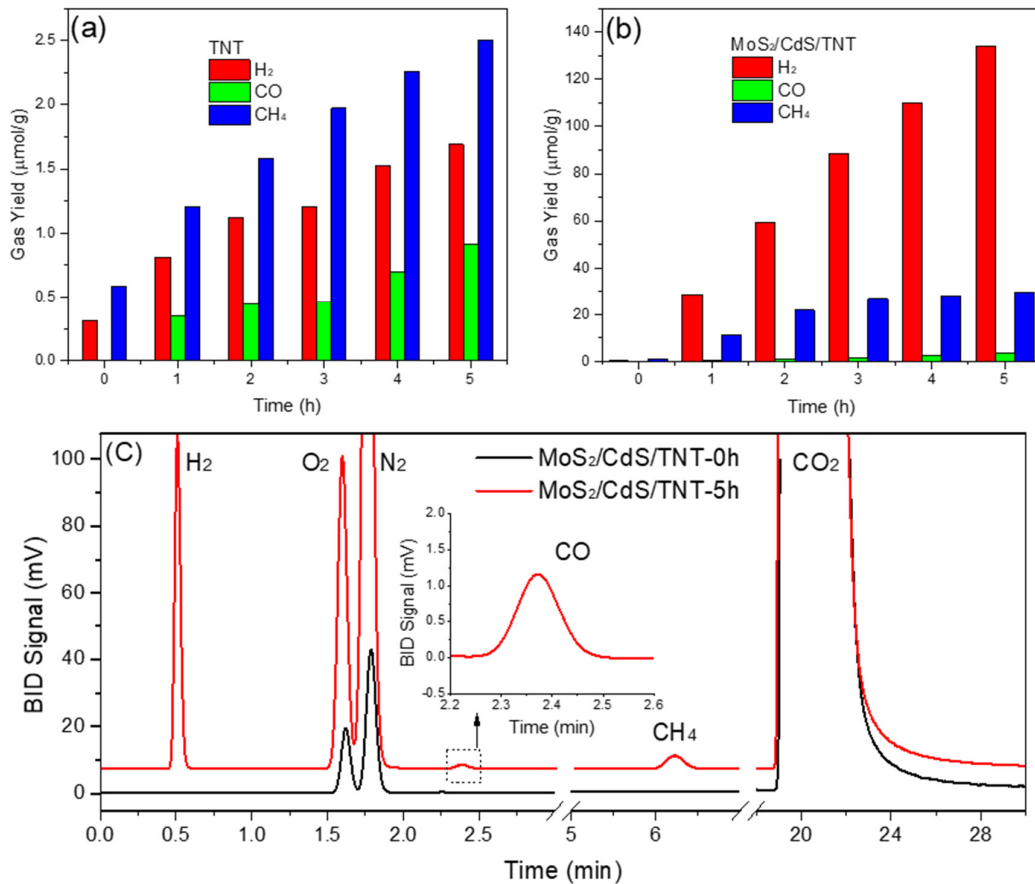
Figure 2-19 (a) Gases yield of pristine TNT, (b) gases yield of MoS2/CdS/TNT as the function of illumination time, (c) gas chromatography peaks of MoS2/CdS/TNT at the illumination time of 0 h and 5 h.

The performance of MoS$_2$/CdS/TNT heterojunction photocatalysts was evaluated for converting CO$_2$ into CH$_4$. Figure 2-19 (a) shows the different gases yield by pristine TNT as a function of illumination time. The amount yield of H$_2$, CO, and CH$_4$ are 1.69 µmol/g, 0.91 µmol/g, and 2.50 µmol/g after illumination for 5 hours. The calculated yield rates are 0.34 µmol/g/h, 0.18 µmol/g/h, and 0.63 µmol/g/h for H$_2$, CO, and CH$_4$. However, MoS$_2$/CdS/TNT heterojunction photocatalysts present an enhanced photocatalytic activity, shown in Figure 2-19 (b). The gas yield rates are 22.79 µmol/g/h, 0.69 µmol/g/h,

and 5.96 µmol/g/h for H_2, CO, and CH_4. Therefore, the specific photocatalytic activities of MoS_2/CdS/TNT heterojunction photocatalysts are 67.4 times, 3.8 times, and 11.9 times larger than that of pristine TNT for the gas yield of H_2, CO, and CH_4. Figure 2-19 (c) shows gas chromatography peaks of MoS_2/CdS/TNT heterojunction photocatalysts measured at the illumination time of 0 h and 5 h.
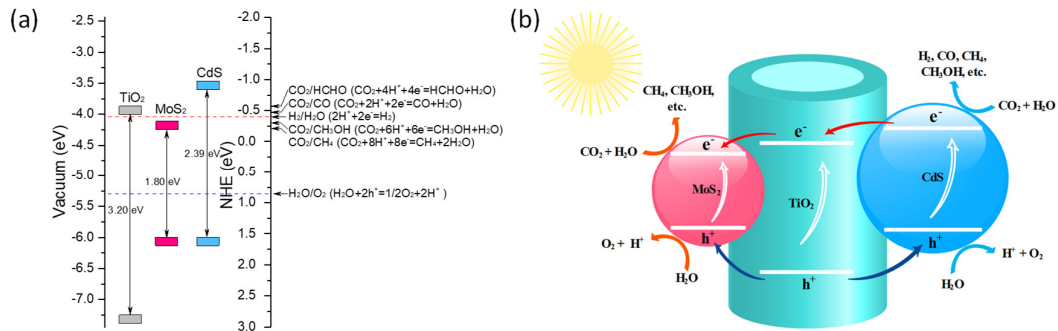
Figure 2-20 (a) band-edge positions of TiO_2, MoS_2, and CdS, and possible reactions related to the photocatalytic conversion of CO_2 with H_2O, (b) illustration of MoS_2/CdS/TNT heterojunction photocatalysts for promoting the charge separation for the photocatalytic conversion of CO_2 with H_2O.

Figure 2-20 (a) shows the band-edge positions of TiO_2, MoS_2, and CdS, and possible reactions related to the photocatalytic conversion of CO_2 with H_2O [127]. In a typical photocatalytic reaction, a variety of products (such as CO, HCHO, CH_3OH, CH_4, or higher hydrocarbons) may be formed in the reduction of CO_2 with H_2O. Apparently, the conduction band edge of CdS is higher than the redox potentials of CO_2 reduction; therefore, various products (H_2, CO, CH_3OH, CH_4, etc.) may produce on the deposited CdS layer. However, conduction bands of TiO_2 and MoS_2 are close to the redox potentials of CO_2/CH_3OH, CO_2/CH_4, and H_2/H_2O, CO or HCHO may hard to produce on TiO_2 and MoS_2 materials. Figure 2-20 (b) shows an illustration of MoS_2/CdS/TNT heterojunction photocatalysts for promoting the charge separation for the photocatalytic conversion of CO_2 with H_2O. Under illumination, electron-hole pairs are generated on MoS_2/CdS/TNT heterojunction nanocomposites after absorbing the energy from light. The small amounts of electron-hole pairs are separated and transported on the surface of catalysts

to participate in redox reactions. The stepped conduction bands combination on MoS_2/CdS/TNT nanocomposites are liable to electrons cascading from CdS to MoS_2, reducing the recombination of electron-hole.

Conclusions

TNT electrodes have been fabricated by electrochemical anodization. Metal sulfide nanomaterials, (MoS_2 and CdS nanoparticles) are deposited on TNT by magnetron sputter technique. The performance of as-synthesized MoS_2/CdS/TNT heterojunction photocatalysts are evaluated by CO_2 conversion, showing the enhanced specific photocatalytic activities which are 97 times, 3.8 times, and 15 times larger than that of pristine TNT for the yields of H_2, CO, and CH_4. This work may have the potential to provide new insights into the development of visible-light-driven nanocomposites as highly efficient photocatalysts for converting CO_2 into fuels.

2.3 Multiple-heterojunction TiO₂ nanotube electrode

2.3.1 PbS quantum dots/Au/Ti³⁺ sites/TiO₂ heterojunction (Article 6)

Motivation

This work is performed after the study in Article 1, Article 2, and Article 4. From these articles, absorption, generation and transportation have been improved by introducing heterojunction materials, such as PbS QDs, CdSe QDs, and Ti^{3+} sites. However, a larger amount of generated electron-hole pairs are recombined in bulk or on the surface of TiO_2 nanomaterials, shown in Figure 1-4. The motivation of this work is to reduce the recombination of electron-hole by heterojunction engineering.

Experiments

TNT electrodes were fabricated by electrochemical anodization of Ti foil in a fluoride-containing electrolyte. The electrodes were annealed at 500˚C (LENTON WHT6) for 3 h in air to form anatase TNT. Ti^{3+}/TNT were obtained by electrochemical reduction in 0.5

M Na$_2$SO$_4$ electrolyte under the applied potential of 5 V for 15 seconds. Au NPs were loaded on Ti^{3+}/TNT by magnetron sputtering deposition under the deposition current of 15 mA for 70 seconds (denoted as Ti^{3+}/TNT-Au). OA-capped PbS QDs were loaded on the Ti^{3+}/TNT-Au by dipping process (denoted as Ti^{3+}/TNT-Au-PbS). PbS QDs/Au/Ti^{3+}/TNT heterojunction electrodes were formed after ethanol volatilizing. Schematic diagram of Ti^{3+}/TNT-Au-PbS heterojunction electrode fabrication procedures is shown in Figure 2-21.

Au Nanoparticle   PbS Quantum dot
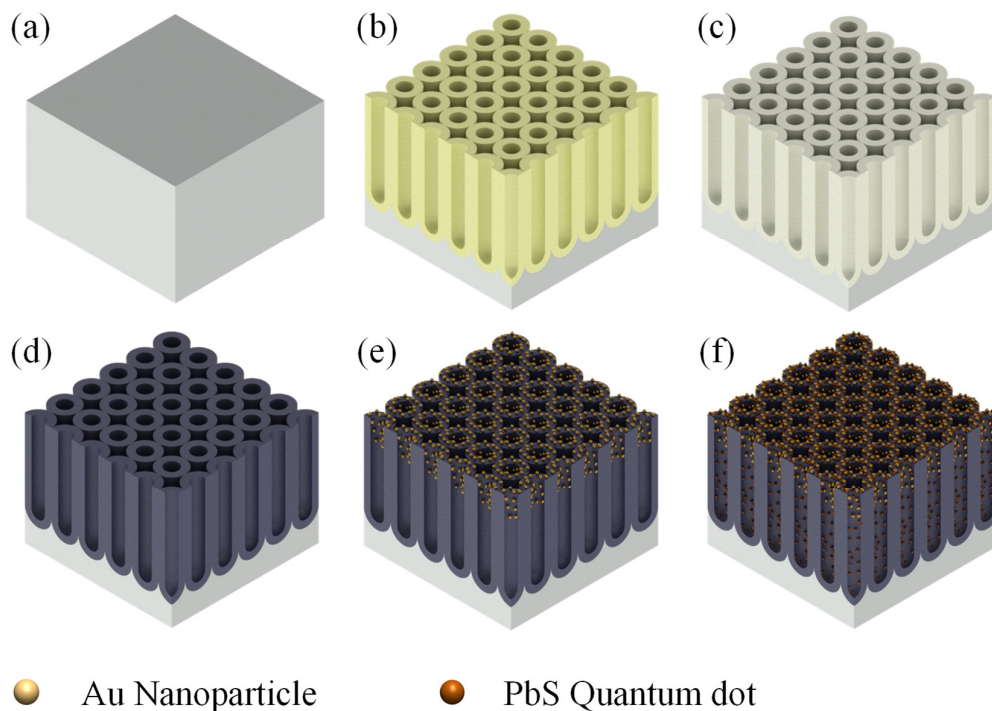
Figure 2-21 Schematic diagram of Ti^{3+}/TNT-Au-PbS heterojunction electrode fabrication procedures: (a) Ti foil, (b) anodization to form TNT, (c) annealing to form anatase phase, (d) electrochemical reduction to obtain black TNT, (e) loading Au NPs by magnetron sputter technique, and (f) loading PbS QDs by dip coating approach.

Results and discussion

Figure 2-22 shows SEM images of TNT, TNT-Au, TNT-Au-PbS, Ti^{3+}/TNT, Ti^{3+}/TNT-Au, and Ti^{3+}/TNT-Au-PbS. In Figure 2-22 (a), TNT presents a porous periodical structure with an

average diameter of ~130 nm and a wall thickness of ~15 nm. After loading with nanoparticles Au, the inner diameter decreases to ~115 nm and its wall thickness increases to ~20 nm, shown in Figure 2-22 (b). Further loading with quantum dots PbS, some clusters (~30 nm) are observed in the inset of Figure 2-22 (c), and they randomly distribute on the TNT walls. No obvious morphological differences between TNT and Ti^{3+}/TNT, as shown in Figure 2-22 (d). Figure 2-22 (e) and Figure 2-22 (f) illustrate the similar surface morphologies to those of TNT-Au and TNT-Au-PbS.
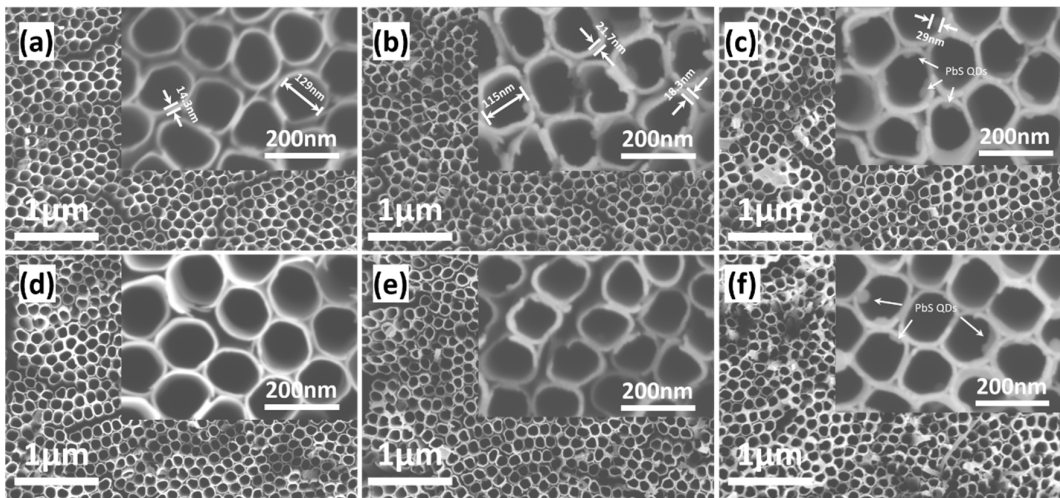
Figure 2-22 SEM images of (a) TNT, (b) TNT-Au, (c) TNT-Au-PbS, (d) Ti^{3+}/TNT, (e) Ti^{3+}/TNT-Au, and (f) Ti^{3+}/TNT-Au-PbS.

Figure 2-23 (a) shows UV-vis absorption spectra of UV-vis absorption spectra of TNT, TNT-Au, TNT-Au-PbS, Ti^{3+}/TNT, Ti^{3+}/TNT-Au and Ti^{3+}/TNT-Au-PbS electrodes. TNT electrodes show weak absorption at the visible light above ~400 nm, but Ti^{3+}/TNT electrodes display strong absorption in this regime. After loading with Au NPs, Ti^{3+}/TNT-Au shows further enhancement from 325 nm to 615 nm. However, the absorption of Ti^{3+}/TNT-Au-PbS decreases from wavelength 480 nm to 850 nm because of some light may scatter by Nafion layer which used as a binder for preparing PbS QDs solution [128]. Figure 2-23 (b) shows transient photocurrent responses of as-prepared samples under visible illumination at the applied potential of +1 V. The photocurrent density on fifth pulse for TNT, TNT-Au, TNT-Au-PbS, Ti^{3+}/TNT, Ti^{3+}/TNT-Au and Ti^{3+}/TNT-Au-PbS are 0.592 mA/cm^2, 0.616 mA/cm^2, 0.646 mA/cm^2, 0.789 mA/cm^2, 0.999 mA/cm^2, and 1.149

mA/cm^2 under visible light. Obviously, the photocurrent densities of TNT-Au and TNT-Au-PbS are enhanced by 4.05% and 4.87% as compared to that of as-prepared TNT. However, the photocurrent of Ti^{3+}/TNT-Au and Ti^{3+}/TNT-Au-PbS are enhanced by 26.62% and 15.92% of Ti^{3+}/TNT. Interestingly, we found that photocurrent density of Ti^{3+}/TNT is 33.28% higher than that of pristine TNT. The photocurrent enhancements of Ti^{3+}/TNT-Au and Ti^{3+}/TNT-Au-PbS are 62.18% and 77.86% higher than that of TNT-Au, TNT-Au-PbS.
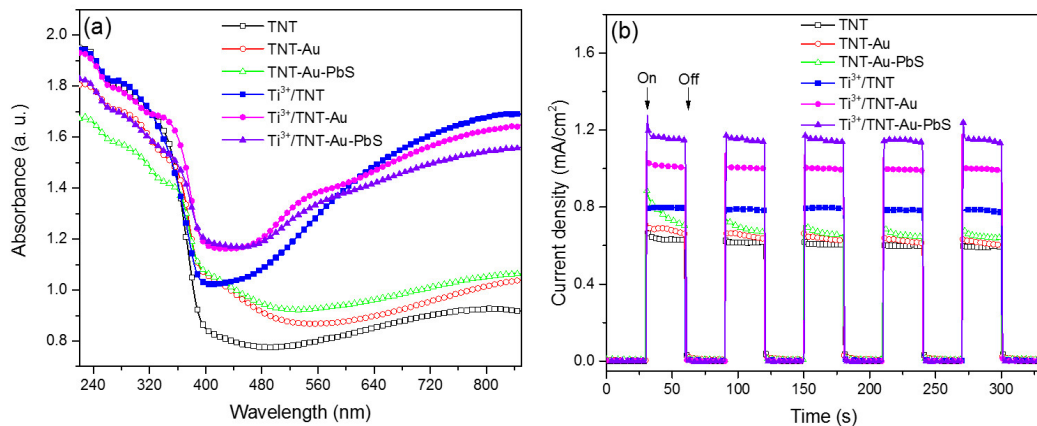
Figure 2-23 (a) UV-vis absorption spectra of TNT, TNT-Au, TNT-Au-PbS, Ti^{3+}/TNT, Ti^{3+}/TNT-Au and Ti^{3+}/TNT-Au-PbS, (b) transient photocurrent responses of as-prepared samples under visible illumination at the applied potential of +1 V.
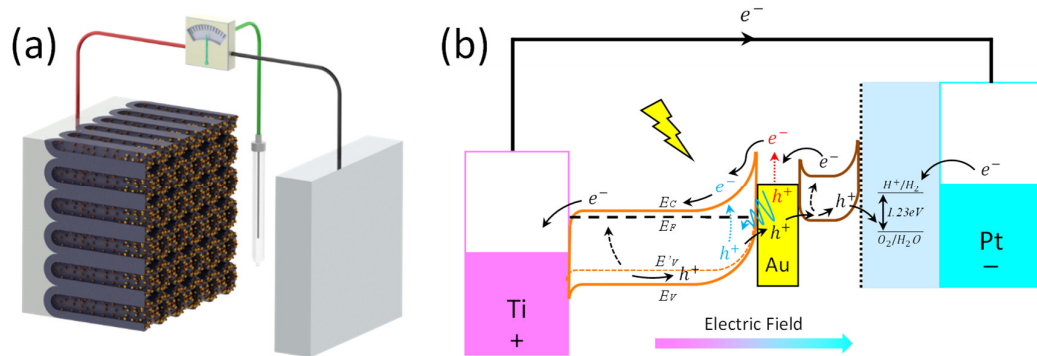
Figure 2-24 (a) schematic setup of electrochemical measurements for Ti^{3+}/TNT-Au-PbS heterojunction electrode in 0.5 M Na$_2$SO$_4$ solution, (b) band diagram of Ti^{3+}/TNT-Au-PbS heterojunction electrode in the positive bias potential under visible light illumination.

Figure 2-24 (a) shows the schematic setup of electrochemical measurements for evaluating the Ti^{3+}/TNT-Au-PbS heterojunction electrode in 0.5 M Na$_2$SO$_4$, and Figure 2-24 (b) shows band diagram of Ti^{3+}/TNT-Au-PbS electrode in the positive bias potential under visible light illumination. Under visible illumination, the photogenerated electrons on Ti^{3+}/TNT, Au NPs, and PbS QDs are cascade down to Ti foil. Meanwhile, holes are pushed to the valence band of PbS QDs under positive bias potential. Also, electrons generated on Au NPs usually transfer to Ti^{3+}/TNT by two ways: hot electron injection (HEI) and plasmonic resonance energy transfer (PRET) [129-130]. Au NPs could play as main carrier trapping centers for further reactions.

Conclusions

TiO$_2$ nanotubes (TNT) have been fabricated by electrochemical anodization and then subsequently reduced them as black TiO$_2$ nanotubes by an electrochemical method in 0.5 M Na$_2$SO$_4$ solution. The black TNT show a high light absorption from the wavelength 400 nm to 850 nm. To retard photo-generated carrier recombination, Au nanoparticles (NPs) and PbS quantum dots (QDs) were loaded on as-prepared and black TNT by magnetron sputtering technique and dip-coating approach. The photocurrent densities of Ti^{3+}/TNT-Au (0.999 mA/cm^2) and Ti^{3+}/TNT-Au-PbS (1.149 mA/cm^2) are enhanced by 62.18% and 77.86% as compared with the as-prepared TNT samples. However, the photocurrent densities of as-prepared TNT samples are only increased about 4.05% and 4.87% after loaded with the same amount of Au NPs and PbS QDs. Therefore, the loaded Au NPs and PbS QDs on black TNT could consider as separation centers rather than light absorbers for accelerating carrier separation.

3　Conclusions

This thesis aims to synthesize high-performance TiO$_2$ nanotubes-based electrode by heterojunction engineering for improving solar energy utilization, conversion, and storage. From photo-energy conversion mechanism, several types of heterogeneous materials are loaded on TiO$_2$ nanotubes to synthesize multiple-heterojunction nanocomposites for improving light absorption, photo-induced charge generation, separation, and transport. The main conclusions are summarized in the following aspects:

- Ti^{3+} sites are introduced into pristine TiO$_2$ nanotubes by electrochemical cathodic reduction. The introduced Ti^{3+} sites bring two advantages: (1) the "black" of Ti^{3+}/TNT exhibits excellent light absorption in the visible or even infrared regime; (2) an improved conductivity of Ti^{3+}/TNT is beneficial to photo-induced charge transport.

- TiN layer is conformally coated on pristine TNT by atomic layer deposition (ALD) technique. The TiN/TNT heterojunction electrode has a superior conductivity which is also favorable for photo-induced charge transport.

- Quantum dots (PbS and CdSe) are loaded on pristine TNT and Ti^{3+}/TNT by the ultrasonic-assisted dip-coating process. The loaded PbS QDs and CdSe QDs firstly play as light absorbers for enhancing absorption in visible regime. Then, the formed heterogeneous band diagrams on PbS QDs/TNT and CdSe QDs/Ti^{3+}/TNT are liable to photo-induced charges separation.

- Au nanoparticles are loaded on Ti^{3+}/TNT by magnetron sputtering technique. Au NPs contribute extra photo-induced charges by hot electron injection (HEI) and plasmonic resonance energy transfer (PRET). Also, Schottky junction between Au NPs and Ti^{3+}/TNT could accelerate the separation of photo-induced charges.

- Metallic sulfides (MoS$_2$ and CdS) are deposited on pristine TNT by magnetron sputtering technique. The narrowed bandgaps of MoS$_2$ and CdS facilitate to capture the energy of photons from sunlight and generate more photo-induced charges. The match of conduction band-edges of MoS$_2$, CdS, and TiO$_2$ are apt to

photo-induced charges separation and transport, and to meet the potentials of redox reactions for producing solar fuels.

Based on the synthesized heterojunction materials, several applications are conducted in the field of electricity storage, photoelectric conversion, and solar fuels conversion. The applications are described as follows:

- Ti^{3+}/TNT was used as supercapacitor electrode based on its high specific surface and improved conductivity. The capacitance of Ti^{3+}/TNT (14.3 mF/cm^2) is increased by ~14 times larger than that of pristine TNT (1.02 mF/cm^2). Furthermore, the extra capacitance (43.4%) is contributed by surface morphologies control of "nano grass" on the electrode. TiN/TNT was also used as supercapacitor electrode, exhibiting an enhanced capacitance. Importantly, TiN/TNT present outstanding cycling stability with 98.5% retention of original specific capacitance after 2000 cycles.

- PbS QDs/TNT, CdSe QDs/Ti^{3+}/TNT, and PbS QDs/Au/Ti^{3+}/TNT were used as photoelectrodes for measuring fundamental photoelectric characteristics. The enhanced photocurrents are attributed to the improvements in light absorption, charges generation, separation, and transport. The systematic investigations on these photoelectrodes may show a potential application in photo-detectors, photovoltaic, and photo water-splitting.

- MoS$_2$/CdS/TNT was applied as photocatalyst, and its photocatalytic performance was evaluated by converting CO$_2$ with H$_2$O into CH$_4$. The H$_2$, CO, and CH$_4$ yields of MoS$_2$/CdS/TNT are 67.4 times, 3.8 times, and 11.9 times larger than that of pristine TNT. This work may have the potential to provide new insights into the development of visible-light-driven nanocomposites as highly efficient photocatalysts for converting CO$_2$ into fuels.

References

[1] L. Pérez-Lombard, J. Ortiz, C. Pout, A review on buildings energy consumption information. *Energy and Buildings*. **40**, 394–398 (2008). DOI: 10.1016/j.enbuild.2007.03.007.

[2] P. V. Kamat, Meeting the clean energy demand: Nanostructure Architectures for Solar Energy Conversion. *Journal of Physical Chemistry C*. **392**, 2834–2860 (2007). DOI: 10.1002/adma.200902096.

[3] A. Goldthau, The G20 must govern the shift to low-carbon energy. *Nature*. **546**, 203–205 (2017). DOI: 10.1038/546203a.

[4] S. Chu, A. Majumdar, Opportunities, and challenges for a sustainable energy future. *Nature*. **488**, 294–303 (2012). DOI: 10.1038/nature11475.

[5] S. Chu, Y. Cui, N. Liu, The path towards sustainable energy. *Nature Materials*. **16**, 16–22 (2016). DOI: 10.1038/nmat4834.

[6] J. Schmale, D. Shindell, E. Von Schneidemesser, I. Chabay, M. Lawrence, Air pollution: Clean up our skies. *Nature*. **515**, 335–337 (2014). DOI: 10.1038/515335a.

[7] D. S. Sholl, R. P. Lively, Seven chemical separations to change the world. *Nature*. **532**, 435–437 (2016). DOI: 10.1038/532435a.

[8] H. Toros, M. Abbasnia, M. Sagdic, M. Tayanç, Long-Term Variations of Temperature and Precipitation in the Megacity of Istanbul for the Development of Adaptation Strategies to Climate Change, Advances in Meteorology. (2017). DOI: 10.1155/2017/6519856.

[9] International Energy Agency, Energy and Air Pollution. *World Energy Outlook - Special Report*, 266 (2016).

[10] A. M. Omer, Energy, environment and sustainable development. *Renewable and Sustainable Energy Reviews*. **12**, 2265–2300 (2008). DOI: 10.1016/j.rser.2007.05.001.

[11]   P. A. Owusu, S. Asumadu-Sarkodie, A review of renewable energy sources, sustainability issues and climate change mitigation. *Cogent Engineering*. **3**, 1–14 (2016). DOI: 10.1080/23311916.2016.1167990.

[12]   Energy for a Sustainable Future. *The Secretary-General's Advisory Group on Energy and Climate Change*, 44 (2010).

[13]   M. A. Green, S. P. Bremner, Energy conversion approaches and materials for high-efficiency photovoltaics. *Nature Materials*. **16**, 23–34 (2016). DOI: 10.1038/nmat4676.

[14]   M. R. Islam, S. Mekhilef, R. Saidur, Progress and recent trends of wind energy technology. *Renewable and Sustainable Energy Reviews*. **21**, 456–468 (2013). DOI: 10.1016/j.rser.2013.01.007.

[15]   E. Callaway, Energy: To catch a wave. *Nature*. **450**, 156–159 (2007). DOI: 10.1038/450156a.

[16]   J. W. Lund, T. L. Boyd, Direct utilization of geothermal energy 2015 worldwide review. *Geothermics*. **60**, 66–93 (2016). DOI: 10.1016/j.geothermics.2015.11.004.

[17]   N. S. Lewis, Toward Cost-Effective Solar Energy Use. *Science*. **315**, 798–801 (2007). DOI: 10.1126/science.1137014.

[18]   M. A. Green, A. Ho-Baillie, H. J. Snaith, The emergence of perovskite solar cells. *Nature Photonics*. **8**, 506–514 (2014). DOI: 10.1038/nphoton.2014.134.

[19]   Y. Tian, C. Y. Zhao, A review of solar collectors and thermal energy storage in solar thermal applications. *Applied Energy*. **104**, 538–553 (2013). DOI: 10.1016/j.apenergy.2012.11.051.

[20]   Y. Tachibana, L. Vayssieres, J. R. Durrant, Artificial photosynthesis for solar water-splitting. *Nature Photonics*. **6**, 511–518 (2012). DOI: 10.1038/nphoton.2012.175.

[21]   M. Neises, S. Tescari, L. de Oliveira, M. Roeb, C. Sattler, B. Wong, Solar-heated rotary kiln for thermochemical energy storage. *Solar Energy*. **86**, 3040–3048 (2012). DOI: 10.1016/j.solener.2012.07.012.

[22]   I. Roger, M. A. Shipman, M. D. Symes, Earth-abundant catalysts for electrochemical and photoelectrochemical water splitting. *Nature Reviews Chemistry*. **1** (2017). DOI: 10.1038/s41570-016-0003.

[23]   J. A. Herron, J. Kim, A. A. Upadhye, G. W. Huber, C. T. Maravelias, A general framework for the assessment of solar fuel technologies. *Energy & Environmental Science.* **8**, 126–157 (2015). DOI: 10.1039/C4EE01958J.

[24]   J. H. Montoya, Linsey C. Seitz, Pongkarn Chakthranont, Aleksandra Vojvodic, Thomas F. Jaramillo, Jens K. Nørskov. Materials for solar fuels and chemicals. *Nature Materials*. **16**, 70–81 (2016). DOI: 10.1038/nmat4778.

[25]   K. Sivula, R. Van De Krol, Semiconducting materials for photoelectrochemical energy conversion. *Nature Reviews Materials*. **1** (2016). DOI: 10.1038/natrevmats.2015.10.

[26]   F. von Bichowsky, Titanium White - A New Method for its Preparation. *Industrial and Engineering Chemistry*. **21**, 1061–1063 (1929). DOI: 10.1021/ie50239a021.

[27]   A. Fujishima, K. Honda, Electrochemical photolysis of water at a semiconductor electrode. *Nature*. **238**, 37–38 (1972). DOI: 10.1038/238037a0.

[28]   B. O'Regan, M. Gratzel, A Low-Cost, High-Efficiency Solar-Cell Based on Dye-Sensitized Colloidal TiO$_2$ Films. *Nature*. **353**, 737–740 (1991). DOI: 10.1038/353737a0.

[29]   M. Ni, M. K. H. Leung, D. Y. C. Leung, K. Sumathy, A review and recent developments in photocatalytic water-splitting using TiO$_2$ for hydrogen production. *Renewable and Sustainable Energy Reviews*. **11**, 401–425 (2007). DOI: 10.1016/j.rser.2005.01.009.

[30]   K. I. Ishibashi, A. Fujishima, T. Watanabe, K. Hashimoto, Detection of active oxidative species in TiO$_2$ photocatalysis using the fluorescence technique. *Electrochemistry Communications*. **2**, 207–210 (2000). DOI: 10.1016/S1388-2481(00)00006-0.

[31]   G. Armstrong, A. R. Armstrong, P. G. Bruce, P. Reale, B. Scrosati, TiO$_2$(B) nanowires as an improved anode material for lithium-ion batteries containing LiFePO$_4$ or LiNi$_{0.5}$Mn$_{1.5}$O$_4$ cathodes and a polymer electrolyte. *Advanced Materials*. **18**, 2597–2600 (2006). DOI: 10.1002/adma.200601232.

[32]   X. Lu, M. Yu, G. Wang, T. Zhai, S. Xie, Y. Ling, Y. Tong, Y. Li, H-TiO$_2$@MnO$_2$/H-TiO$_2$@C core-shell nanowires for high performance and flexible asymmetric supercapacitors. *Advanced Materials*. **25**, 267–272 (2013). DOI: 10.1002/adma.201203410.

[33]   C. Zhang, H. Yu, Y. Li, Y. Gao, , Y. Zhao, W. Song, Z. Shao, B. Yi, Supported noble metals on hydrogen-treated TiO$_2$ nanotube arrays as highly ordered electrodes for fuel cells. *ChemSusChem*. **6**, 659–666 (2013). DOI: 10.1002/cssc.201200828.

[34]   W. Zhao, W. Ma, C. Chen, J. Zhao, Z. Shuai, Efficient Degradation of Toxic Organic Pollutants with Ni$_2$O$_3$/TiO$_{2-x}$B$_x$ under Visible Irradiation. *Journal of the American Chemical Society*. **126**, 4782–4783 (2004). DOI: 10.1021/ja0396753.

[35]   H. Tang, K. Prasad, R. Sanjines, F. Levy, TiO$_2$ Anatase Thin-Films As Gas Sensors. *Sensors and Actuators B-Chemical*. **26** (1995), pp. 71–75. DOI: 10.1016/0925-4005(94)01559-z.

[36]   S. Wu, Z. Weng, X. Liu, K. W. K. Yeung, P. K. Chu, Functionalized TiO$_2$ based nanomaterials for biomedical applications. *Advanced Functional Materials*. **24**, 5464–5481 (2014). DOI: 10.1002/adfm.201400706.

[37]   J. Schneider, M. Matsuoka, M. Takeuchi, J. Zhang, Y. Horiuchi, M. Anpo, D. W. Bahnemann, Understanding TiO$_2$ Photocatalysis: Mechanisms and Materials. *Chemical Reviews*. **114**, 9919–9986 (2014). DOI: 10.1021/cr5001892.

[38]   K. Hashimoto, H. Irie, A. Fujishima, TiO$_2$ Photocatalysis: A Historical Overview and Future Prospects. *Japanese Journal of Applied Physics*. **44**, 8269–8285 (2005). DOI: 10.1143/JJAP.44.8269.

[39]   J. Ni, S. Fu, C. Wu, J. Maier, Y. Yu, L. Li, Self-Supported Nanotube Arrays of Sulfur-

Doped TiO_2 Enabling Ultrastable and Robust Sodium Storage. *Advanced Materials*. **28**, 2259–2265 (2016). DOI: 10.1002/adma.201504412.

[40] M. Landmann, E. Rauls, W. G. Schmidt, The electronic structure and optical response of rutile, anatase and brookite TiO_2. *Journal of Physics Condensed Matter*. **24** (2012), DOI: 10.1088/0953-8984/24/19/195503.

[41] J. Zhang, P. Zhou, J. Liu, J. Yu, New understanding of the difference of photocatalytic activity among anatase, rutile and brookite TiO_2. *Physical Chemistry Chemical Physics.* **16**, 20382–20386 (2014). DOI: 10.1039/C4CP02201G.

[42] W. J. Yin, H. Tang, S. H. Wei, M. M. Al-Jassim, J. Turner, Y. Yan, Band structure engineering of semiconductors for enhanced photoelectrochemical water splitting: The case of TiO_2. *Physical Review B - Condensed Matter and Materials Physics*. **82**, 1–6 (2010). DOI: 10.1103/PhysRevB.82.045106.

[43] J. S. Lee, K. H. You, C. B. Park, Highly photoactive, low bandgap TiO_2 nanoparticles wrapped by graphene. *Advanced Materials*. **24**, 1084–1088 (2012). DOI: 10.1002/adma.201104110.

[44] A. G. Kontos, A. I. Kontos, D. S. Tsoukleris, V. Likodimos, J. Kunze, , P. Schmuki, P. Falaras, Photo-induced effects on self-organized TiO_2 nanotube arrays: The influence of surface morphology. *Nanotechnology*. **20** (2009), DOI: 10.1088/0957-4484/20/4/045603.

[45] C. Di Valentin, G. Pacchioni, Trends in non-metal doping of anatase TiO_2: B, C, N and F. *Catalysis Today*. **206**, 12–18 (2013). DOI: 10.1016/j.cattod.2011.11.030.

[46] L. G. Devi, R. Kavitha, A review on non metal ion doped titania for the photocatalytic degradation of organic pollutants under UV/solar light: Role of photogenerated charge carrier dynamics in enhancing the activity. *Applied Catalysis B: Environmental*. **140**–**141**, 559–587 (2013). DOI: 10.1016/j.apcatb.2013.04.035.

[47] R. Asahi, Visible-Light Photocatalysis in Nitrogen-Doped Titanium Oxides. *Science*. **293**, 269–271 (2001). DOI: 10.1126/science.1061051.

[48] S. U. M. Khan, Efficient Photochemical Water Splitting by a Chemically Modified n-TiO$_2$. *Science*. **297**, 2243–2245 (2002). DOI: 10.1126/science.1075035.

[49] J. Choi, H. Park, M. R. Hoffmann, Effects of Single Metal-Ion Doping on the Visible-Light Photoreactivity of TiO$_2$, *The Journal of Physical Chemistry C.* **114**, 783–792 (2016). DOI: 10.1021/jp908088x.

[50] W. Choi, A. Termin, M. R. Hoffmann, The Role of Metal Ion Dopants in Quantum-Sized TiO$_2$: Correlation between Photoreactivity and Charge Carrier Recombination Dynamics. *The Journal of Physical Chemistry*. **98**, 13669–13679 (1994). DOI: 10.1021/j100102a038.

[51] Y. Sakatani, H. Ando, K. Okusako, H. Koike, J. Nunoshige, T. Takata, Junko N. Kondo, M. Hara, K. Domen, Metal ion and N co-doped TiO$_2$ as a visible-light photocatalyst. *Journal of Materials Research*. **19**, 2100–2108 (2004). DOI: 10.1557/JMR.2004.0269.

[52] R. Dholam, N. Patel, M. Adami, A. Miotello, Hydrogen production by photocatalytic water-splitting using Cr- or Fe-doped TiO$_2$ composite thin films photocatalyst. *International Journal of Hydrogen Energy*. **34**, 5337–5346 (2009). DOI: 10.1016/j.ijhydene.2009.05.011.

[53] D. Buso, J. Pacifico, A. Martucci, P. Mulvaney, Gold-nanoparticle-doped TiO$_2$ semiconductor thin films: Optical characterization. *Advanced Functional Materials*. **17**, 347–354 (2007). DOI: 10.1002/adfm.200600349.

[54] S, Sakthivel, M. V. Shankar, M. Palanichamy, B. Arabindoo, D. W. Bahnemann, V. Murugesan. Enhancement of photocatalytic activity by metal deposition: Characterisation and photonic efficiency of Pt, Au and Pd deposited on TiO$_2$ catalyst. *Water Research*. **38**, 3001–3008 (2004). DOI: 10.1016/j.watres.2004.04.046.

[55]   F. Xiao, Layer-by-layer self-assembly construction of highly ordered metal TiO$_2$ nanotube arrays heterostructures (M/TNT, M = Au, Ag, Pt) with tunable catalytic activities. *Journal of Physical Chemistry C*. **116**, 16487–16498 (2012). DOI: 10.1021/jp3034984.

[56]   H. Lee, H. C. Leventis, S. J. Moon, P. Chen, S. Ito, S. A. Haque, T. Torres, F. Nüesch, T. Geiger, S. M. Zakeeruddin, M. Grätzel, M. K. Nazeeruddin, PbS and CdS quantum dot-sensitized solid-state solar cells: "Old concepts, new results." *Advanced Functional Materials*. **19**, 2735–2742 (2009). DOI: 10.1002/adfm.200900081.

[57]   L. X. Yang, S. L. Luo, Y. Li, Y. Xiao, Q. Kang, Q. Y. Cai, High Efficient Photocatalytic Degradation of p-Nitrophenol on a Unique Cu$_2$O/TiO$_2$ p-n Heterojunction Network Catalyst. *Environmental Science and Technology*. **44**, 7641–7646 (2010). DOI: 10.1021/es101711k.

[58]   W. T. Sun, A. Yu, H. Y. Pan, X. F. Gao, Q. Chen, L. M. Peng, CdS quantum dots sensitized TiO$_2$ nanotube-array photoelectrodes. *Journal of the American Chemical Society*. **130**, 1124–1125 (2008). DOI: 10.1021/ja0777741.

[59]   J. M. Nedeljković, O. I. Mićić, S. P. Ahrenkiel, A. Miedaner, A. J. Nozik, Growth of InP Nanostructures via Reaction of Indium Droplets with Phosphide Ions: Synthesis of InP Quantum Rods and InP-TiO$_2$ Composites. *Journal of the American Chemical Society*. **126**, 2632–2639 (2004). DOI: 10.1021/ja039311a.

[60]   Q. Xiang, J. Yu, M. Jaroniec, Synergetic effect of MoS$_2$ and graphene as cocatalysts for enhanced photocatalytic H$_2$ production activity of TiO$_2$ nanoparticles. *Journal of the American Chemical Society*. **134**, 6575–6578 (2012). DOI: 10.1021/ja302846n.

[61]   P. C. Ricci, C. M. Carbonaro, L. Stagi, M. Salis, A. Casu, S. Enzo, F. Delogu, Anatase-to-rutile phase transition in TiO$_2$ nanoparticles irradiated by visible light. *Journal of Physical Chemistry C*. **117**, 7850–7857 (2013). DOI: 10.1021/jp312325h.

[62]   Y. Zhou, M. Antonietti, Synthesis of Very Small TiO$_2$ Nanocrystals in a Room-

Temperature Ionic Liquid and Their Self-Assembly toward Mesoporous Spherical Aggregates. *Journal of the American Chemical Society*. **125**, 14960–14961 (2003). DOI: 10.1021/ja0380998.

[63] X. Feng, K. Shankar, O. K. Varghese, M. Paulose, T. J. Latempa, C. Grimes, Vertically aligned single crystal TiO₂ nanowire arrays grown directly on transparent conducting oxide coated glass: synthesis details and applications. *Nano letters*. **8**, 3781–3786 (2008). DOI: 10.1021/nl802096a.

[64] B. Liu, E. S. Aydil, Growth of Oriented Single-Crystalline Rutile TiO₂ Nanorods on Transparent Conducting Substrates for Dye-Sensitized Solar Cells. *Journal of the American Chemical Society*. **131**, 3985–3990 (2009). DOI: 10.1021/ja8078972.

[65] L. Yang, W. W. F. Leung, Application of a bilayer TiO₂ nanofiber photoanode for optimization of dye-sensitized solar cells. *Advanced Materials*. **23**, 4559–4562 (2011). DOI: 10.1002/adma.201102717.

[66] J. Cui, D. Sun, W. Zhou, H. Liu, P. Hu, N. Ren, H. Qin, Z. Huang, J. Lin, H. Ma, Electrocatalytic oxidation of nucleobases by TiO₂ nanobelts. *Physical chemistry chemical physics*. **13**, 9232–7 (2011). DOI: 10.1039/c1cp20082h.

[67] M. Paulose, K. Shankar, S. Yoriya, H. E. Prakasam, O. K. Varghese, G. K. Mor, T. A. Latempa, A. Fitzgerald, C. A. Grimes, Anodic growth of highly ordered TiO₂ nanotube arrays to 134 μm in length. *Journal of Physical Chemistry B*. **110**, 16179–16184 (2006). DOI: 10.1021/jp064020k.

[68] G. K. Mor, O. K. Varghese, M. Paulose, C. A. Grimes, Transparent highly ordered TiO₂ nanotube arrays via anodization of titanium thin films. *Advanced Functional Materials*. **15**, 1291–1296 (2005). DOI: 10.1002/adfm.200500096.

[69] M. Paulose, H. E. Prakasam, O. K. Varghese, L. Peng, K. C. Popat, G. K. Mor, T. A. Desai, C. A. Grimes, TiO₂ nanotube arrays of 1000 μm length by anodization of titanium foil: Phenol red diffusion. *Journal of Physical Chemistry C*. **111**, 14992–14997 (2007). DOI: 10.1021/jp075258r.

[70]   D. Kim, A. Ghicov, S. P. Albu, P. Schmuki, Bamboo-Type TiO$_2$ Nanotubes: Improved Conversion Efficiency in Dye-Sensitized Solar Cells. *Journal of the American Chemical Society*, 16454–16455 (2008). DOI: 10.1155/2007/65073.(5).

[71]   W. Guo, F. Zhang, C. Lin, Z. L. Wang, Direct growth of TiO$_2$ nanosheet arrays on carbon fibers for highly efficient photocatalytic degradation of methyl orange. *Advanced Materials*. **24**, 4761–4764 (2012). DOI: 10.1002/adma.201201075.

[72]   W. Zhou, X. Liu, J. Cui, D. Liu, J. Li, H. Jiang, J. Wang, H. Liu, Control synthesis of rutile TiO$_2$ microspheres, nanoflowers, nanotrees and nanobelts via acid-hydrothermal method and their optical properties. *CrystEngComm*. **13**, 4557 (2011). DOI: 10.1039/c1ce05186e.

[73]   A. P. Alivisatos, Perspectives on the physical chemistry of semiconductor nanocrystals. *Journal of Physical Chemistry*. **100**, 13226–13239 (1996). DOI: 10.1021/jp9535506.

[74]   X. Chen, C. Li, M. Grätzel, R. Kostecki, S. S. Mao, Nanomaterials for renewable energy production and storage. *Chemical Society Reviews*. **41**, 7909 (2012). DOI: 10.1039/c2cs35230c.

[75]   K. Zhu, T. B. Vinzant, N. R. Neale, A. J. Frank, Removing structural disorder from oriented TiO$_2$ nanotube arrays: Reducing the dimensionality of transport and recombination in dye-sensitized solar cells. *Nano Letters*. **7**, 3739–3746 (2007). DOI: 10.1021/nl072145a.

[76]   J. H. Park, S. Kim, A. J. Bard, Novel carbon-doped TiO$_2$ nanotube arrays with high aspect ratios for efficient solar water splitting. *Nano Letters*. **6**, 24–28 (2006). DOI: 10.1021/nl051807y.

[77]   W. N. Wang, W. J. An, B. Ramalingam, S. Mukherjee, D. M. Niedzwiedzki, S. Gangopadhyay, P. Biswas, Size and structure matter: Enhanced CO$_2$ photoreduction efficiency by size-resolved ultrafine Pt nanoparticles on TiO$_2$ single crystals. *Journal of the American Chemical Society*. **134**, 11276–11281 (2012). DOI: 10.1021/ja304075b.

[78]   Z. Liu, X. Zhang, S. Nishimoto, M. Jin, D. A. Tryk, T. Murakami, A. Fujishima, Highly ordered TiO_2 nanotube arrays with controllable length for photoelectrocatalytic degradation of phenol. *Journal of Physical Chemistry C*. **112**, 253–259 (2008). DOI: 10.1021/jp0772732.

[79]   A. L. Linsebigler, G. Lu, J. T. Yates, Photocatalysis on TiO_2 Surfaces: Principles, Mechanisms, and Selected Results. *Chemical Reviews*. **95**, 735–758 (1995). DOI: 10.1021/cr00035a013.

[80]   X. Zhou, N. Liu, P. Schmuki, Photocatalysis with TiO_2 Nanotubes: "Colorful" Reactivity and Designing Site-Specific Photocatalytic Centers into TiO_2 Nanotubes. *ACS Catalysis*. **7**, 3210–3235 (2017). DOI: 10.1021/acscatal.6b03709.

[81]   X. Chen, L. Liu, P. Y. Yu, S. S. Mao, Increasing Solar Absorption for Photocatalysis with Black Hydrogenated Titanium Dioxide Nanocrystals. *Science*. **331**, 746–750 (2011). DOI: 10.1126/science.1200448.

[82]   X. Liu, P. R. Coxon, M. Peters, B. Hoex, J. M. Cole, D. J. Fray, Black silicon: fabrication methods, properties and solar energy applications. *Energy & Environmental Science.* **7**, 3223–3263 (2014). DOI: 10.1039/C4EE01152J.

[83]   S. K. Joung, T. Amemiya, M. Murabayashi, K. Itoh, Mechanistic studies of the photocatalytic oxidation of trichloroethylene with visible-light-driven N-doped TiO_2 photocatalysts. *Chemistry - A European Journal*. **12**, 5526–5534 (2006). DOI: 10.1002/chem.200501020.

[84]   T. Morikawa, R. Asahi, T. Ohwaki, K. Aoki, Y. Taga, Band-Gap Narrowing of Titanium Dioxide by Nitrogen Doping. *Japanese Journal of Applied Physics*. **40**, L561 (2001). DOI: 10.1143/Jjap.40.L561.

[85]   Z. Zhang, J. T. Yates, Direct Observation of Surface-Mediated Electron-Hole Pair Recombination in TiO_2 (110). *Journal of physical chemistry C*. **2**, 3098–3101 (2010). DOI: 10.1021/jp910404e.

[86]   L. Li, P. A. Salvador, G. S. Rohrer, Photocatalysts with internal electric fields.

Nanoscale. **6**, 24–42 (2014). DOI: 10.1039/C3NR03998F.

[87]   G. Dai, J. Yu, G. Liu, Synthesis and enhanced visible-light photoelectrocatalytic activity of p - N junction BiOI/TiO$_2$ nanotube arrays. *Journal of Physical Chemistry C*. **115**, 7339–7346 (2011). DOI: 10.1021/jp200788n.

[88]   H. Chen, S. Chen, X. I. E. Quan, Structuring a TiO$_2$-Based Photonic Crystal Photocatalyst with Schottky Junction for Efficient Photocatalysis. *Environmental Science & Technology*. **44**, 451–455 (2010). DOI: 10.1021/es902712j.

[89]   D. O. Scanlon, C. W. Dunnill, J. Buckeridge, S. A. Shevlin, A. J. Logsdail, S. M. Woodley, C. R. A. Catlow, M. J. Powell, R. G. Palgrave, I. P. Parkin, G. W. Watson. Band alignment of rutile and anatase TiO$_2$. *Nature Materials*. **12**, 798–801 (2013). DOI: 10.1038/nmat3697.

[90]   A. Li, Z. Wang, H. Yin, S. Wang, P. Yan, , B. Huang, X. Wang, R. Li, X. Zong, H. Han, C. Li, 2016. Understanding the anatase-rutile phase junction in charge separation and transfer in a TiO$_2$ electrode for photoelectrochemical water splitting. *Chemical Science*, (2016). DOI: 10.1039/C6SC01611A.

[91]   Y. H. Chang, C. M. Liu, C. Chen, H. E. Cheng, The heterojunction effects of TiO$_2$ nanotubes fabricated by atomic layer deposition on photocarrier transportation direction. *Nanoscale Research Letters*. **7**, 231 (2012). DOI: 10.1186/1556-276X-7-231.

[92]   H. Zhang, X. Lv, Y. Li, Y. Wang, J. Li, P25 graphene composite as a high performance photocatalyst. *ACS Nano*. **4**, 380–386 (2009). DOI: 10.1021/nn901221k.

[93]   M. Anpo, K. Chiba, M. Tomonari, S. Coluccia, M. Che, M. A. Fox, Photocatalysis on native and platinum-loaded TiO$_2$ and ZnO catalysts. Origin of different reactivities on wet and dry metal oxides. *Bulletin of the Chemical Society of Japan*. **64** (1991), pp. 543–551. DOI: 10.1246/bcsj.64.543.

[94]   N. Serpone, D. Lawless, R. Khairutdinov, E. Pelizzetti, Subnanosecond Relaxation Dynamics in TiO$_2$ Colloidal Sols (Particle Sizes Rp = 1.0-13.4 nm). Relevance to

Heterogeneous Photocatalysis. *The Journal of Physical Chemistry*. **99**, 16655–16661 (1995). DOI: 10.1021/j100045a027.

[95] F. Wu, Y. Yu, H. Yang, L. N. German, Z. Li, J. Chen, W. Yang, L. Huang, W. Shi, L. Wang, X. Wang, Simultaneous Enhancement of Charge Separation and Hole Transportation in a TiO_2–$SrTiO_3$ Core–Shell Nanowire Photoelectrochemical System. *Advanced Materials*. **29**, 1–7 (2017). DOI: 10.1002/adma.201701432.

[96] T. Hisatomi, J. Kubota, K. Domen, Recent advances in semiconductors for photocatalytic and photoelectrochemical water splitting. *Chemical Society Review.* **43**, 7520–7535 (2014). DOI: 10.1039/C3CS60378D.

[97] Y. Wu, M. K. Y. Chan, G. Ceder, Prediction of semiconductor band edge positions in aqueous environments from first principles. *Physical Review B - Condensed Matter and Materials Physics*. **83**, 1–7 (2011). DOI: 10.1103/PhysRevB.83.235301.

[98] S. B. Rawal, S. Bera, D. Lee, D. J. Jang, W. I. Lee, Design of visible-light photocatalysts by coupling of narrow bandgap semiconductors and TiO_2: effect of their relative energy band positions on the photocatalytic efficiency. *Catalysis Science & Technology*. **3**, 1822 (2013). DOI: 10.1039/c3cy00004d.

[99] O. Ola, M. M. Maroto-Valer, Review of material design and reactor engineering on TiO_2 photocatalysis for CO_2 reduction. *Journal of Photochemistry and Photobiology C: Photochemistry Reviews*. **24**, 16–42 (2015). DOI: 10.1016/j.jphotochemrev.2015.06.001.

[100] K. Li, X. An, K. H. Park, M. Khraisheh, J. Tang, A critical review of CO_2 photoconversion: Catalysts and reactors. *Catalysis Today*. **224**, 3–12 (2014). DOI: 10.1016/j.cattod.2013.12.006.

[101] S. C. Roy, O. K. Varghese, M. Paulose, C. A. Grimes, Toward Solar Fuels : Photocatalytic Hydrocarbons. *ACS Nano*. **4**, 1259–1278 (2010). DOI: 10.1021/nn9015423.

[102] W. Tu, Y. Zhou, Z. Zou, Photocatalytic conversion of CO_2 into renewable

hydrocarbon fuels: State-of-the-art accomplishment, challenges, and prospects. *Advanced Materials*. **26**, 4607–4626 (2014). DOI: 10.1002/adma.201400087.

[103] S. Sato, T. Arai, T. Morikawa, K. Uemura, T. M. Suzuki, H. Tanaka, T. Kajino, Selective CO_2 conversion to formate conjugated with H_2O oxidation utilizing semiconductor/complex hybrid photocatalysts. *Journal of the American Chemical Society*. **133**, 15240–15243 (2011). DOI: 10.1021/ja204881d.

[104] J. Zou, Q. Zhang, K. Huang, N. Marzari, Ultraviolet photodetectors based on anodic TiO_2 nanotube arrays. *Journal of Physical Chemistry C*. **114**, 10725–10729 (2010). DOI: 10.1021/jp1011236.

[105] J. H. Rhee, C. C. Chung, E. W. G. Diau, A perspective of mesoscopic solar cells based on metal chalcogenide quantum dots and organometal-halide perovskites. *NPG Asia Materials*. **5**, e68 (2013). DOI: 10.1038/am.2013.53.

[106] G. Liu, N. Hoivik, K. Wang, Small diameter TiO_2 nanotubes with enhanced photoresponsivity. *Electrochemistry Communications*. **28**, 107–110 (2013). DOI: 10.1016/j.elecom.2012.12.020.

[107] A. J. Chiquito, C. A. Amorim, O. M. Berengue, L. S. Araujo, E. P. Bernardo, E. R. Leite, Back-to-back Schottky diodes: The generalization of the diode theory in analysis and extraction of electrical parameters of nanodevices. *Journal of Physics: Condensed Matter*. **24** (2012). DOI: 10.1088/0953-8984/24/22/225303.

[108] K. Zhu, N. R. Neale, A. Miedaner, A. J. Frank, Enhanced charge-collection efficiencies and light scattering in dye-sensitized solar cells using oriented TiO_2 nanotubes arrays. *Nano Letters*. **7**, 69–74 (2007). DOI: 10.1021/nl062000o.

[109] X. Wang, Z. Li, W. Xu, S. A. Kulkarni, S. K. Batabyal, S. Zhang, A. Cao, L. Helena Wong, TiO_2 nanotube arrays based flexible perovskite solar cells with transparent carbon nanotube electrode. *Nano Energy*. **11**, 728–735 (2015). DOI: 10.1016/j.nanoen.2014.11.042.

[110] X. Lu, G. Wang, T. Zhai, M., Yu, J. Gan, Y. Tong, Y. Li, Hydrogenated TiO_2 nanotube

arrays for supercapacitors. *Nano Letters*. **12**, 1690–1696 (2012). DOI: 10.1021/nl300173j.

[111] J. Xu, H. Wu, L. Lu, S. F. Leung, D. Chen, X. Chen, Z. Fan, G. Shen, D. Li, Integrated photo-supercapacitor based on Bi-polar TiO$_2$ nanotube arrays with selective one-side plasma-assisted hydrogenation. *Advanced Functional Materials*. **24**, 1840–1846 (2014). DOI: 10.1002/adfm.201303042.

[112] J. H. Lim, J. Choi, Titanium oxide nanowires originating from anodically grown nanotubes: The bamboo-splitting model. *Small*. **3**, 1504–1507 (2007). DOI: 10.1002/smll.200700114.

[113] A. Mazzarolo, K. Lee, A. Vicenzo, P. Schmuki, Anodic TiO$_2$ nanotubes: Influence of top morphology on their photocatalytic performance. *Electrochemistry Communications*. **22**, 162–165 (2012). DOI: 10.1016/j.elecom.2012.05.037.

[114] J. Yan, G. Wu, N. Guan, L. Li, Z. Li, and X. Cao, Understanding the effect of surface/bulk defects on the photocatalytic activity of TiO$_2$: anatase versus rutile. *Physical Chemistry Chemical Physics*. **15**, 10978 (2013). DOI: 10.1039/c3cp50927c.

[115] R. Ren, Z. Wen, S. Cui, Y. Hou, X. Guo, J. Chen, Controllable Synthesis and Tunable Photocatalytic Properties of Ti^{3+}-doped TiO$_2$. *Scientific Reports*. **5**, 10714 (2015). DOI: 10.1038/srep10714.

[116] B. Bharti, S. Kumar, H. N. Lee, R. Kumar, Formation of oxygen vacancies and Ti^{3+} state in TiO$_2$ thin film and enhanced optical properties by air plasma treatment. *Scientific Reports*. **6**, 1–12 (2016). DOI: 10.1038/srep32355.

[117] R. W. Johnson, A. Hultqvist, S. F. Bent, A brief review of atomic layer deposition: From fundamentals to applications. *Materials Today*. **17**, 236–246 (2014). DOI: 10.1016/j.mattod.2014.04.026.

[118] D. Jang, L. R. Meza, F. Greer, J. R. Greer, Fabrication and deformation of three-dimensional hollow ceramic nanostructures. *Nature Materials*. **12**, 893–898

(2013). DOI: 10.1038/nmat3738.

[119] M. N. Solovan, V. V. Brus, E. V. Maistruk, P. D. Maryanchuk, Electrical and optical properties of TiN thin films. *Inorganic Materials*. **50**, 40–45 (2014). DOI: 10.1134/S0020168514010178.

[120] R. M. Nelms, D. R. Cahela, B. J. Tatarchuk, Modeling double-layer capacitor behavior using ladder circuits. *IEEE Transactions on Aerospace and Electronic Systems*. **39**, 430–438 (2003). DOI: 10.1109/TAES.2003.1207255.

[121] H. Cui, W. Zhao, C. Yang, H. Yin, T. Lin, Y. Shan, Y. Xie, H. Gu, F. Huang, Black TiO₂ nanotube arrays for high-efficiency photoelectrochemical water-splitting. *Journal of Materials Chemistry A.* **2**, 8612–8616 (2014). DOI: 10.1039/C4TA00176A.

[122] J. H. Pan, X. Z. Wang, Q. Huang, C. Shen, Z. Y. Koh, Q. Wang, A. Engel, D. W. Bahnemann, Large-scale synthesis of urchin-like mesoporous TiO₂ hollow spheres by targeted etching and their photoelectrochemical properties. *Advanced Functional Materials*. **24**, 95–104 (2014). DOI: 10.1002/adfm.201300946.

[123] S. Linic, P. Christopher, D. B. Ingram, Plasmonic-metal nanostructures for efficient conversion of solar to chemical energy. *Nature Materials*. **10**, 911–921 (2011). DOI: 10.1038/nmat3151.

[124] S. Stankovich, D. A. Dikin, R. D. Piner, K. A. Kohlhaas, A. Kleinhammes, Y. Y. Jia, Y. Wu, S. B. T. Nguyen, R. S. Ruoff, Synthesis of graphene-based nanosheets via chemical reduction of exfoliated graphite oxide. *Carbon*. **45**, 1558–1565 (2007). DOI: 10.1016/j.carbon.2007.02.034.

[125] S. Wu, Z. Zeng, Q. He, Z. Wang, S. J. Wang, Y. Du, Z. Yin, X. Sun, W. Chen, H. Zhang, Electrochemically reduced single-layer MoS₂ nanosheets: Characterization, properties, and sensing applications. *Small*. **8**, 2264–2270 (2012). DOI: 10.1002/smll.201200044.

[126] X. J. Chua, M. Pumera, The effect of varying solvents for MoS₂ treatment on its catalytic efficiencies for HER and ORR. *Physical Chemistry Chemical Physics.* **19**,

6610–6619 (2017). DOI: 10.1039/C6CP08205J.

[127] M. Q. Yang, C. Han, Y. J. Xu, Insight into the Effect of Highly Dispersed MoS$_2$ versus Layer-Structured MoS$_2$ on the Photocorrosion and Photoactivity of CdS in Graphene-CdS-MoS$_2$ Composites. *Journal of Physical Chemistry C*. **119**, 27234–27246 (2015). DOI: 10.1021/acs.jpcc.5b08016.

[128] Z. Xie, T. Navessin, X. Zhao, M. Adachi, Nafion ionomer aggregation and its influence on proton conduction and mass transport in fuel cell catalyst layers. *ECS Transactions*. **16**, 1811–1816 (2008). DOI: Doi 10.1149/1.2982022.

[129] F. Tan, Z. Zeng, Q. He, Z. Wang, S. J. Wang, Y. Du, Z. Yin, X. Sun, W. Chen, H. Zhang, Rough gold films as broadband absorbers for plasmonic enhancement of TiO$_2$ photocurrent over 400-800 nm. *Scientific Reports*. **6**, 1–10 (2016). DOI: 10.1038/srep33049.

[130] Y. Tian, T. Tatsuma, Mechanisms and applications of plasmon-induced charge separation at TiO$_2$ films loaded with gold nanoparticles. *Journal of the American Chemical Society*. **127**, 7632–7637 (2005). DOI: 10.1021/ja042192u.